JOURNAL OF PETROLOGY | VOLUME 47 | NUMBER 12 | PAGES 2369–2403 | 2006 | doi:10.1093/petrology/egl048

Trace Element and Platinum Group Element Distributions and the Genesis of the Merensky Reef, Western Bushveld Complex, South Africa

ALLAN WILSON* AND GORDON CHUNNETT†

SCHOOL OF GEOLOGICAL SCIENCES, UNIVERSITY OF KWAZULU-NATAL DURBAN, SOUTH AFRICA 4041

RECEIVED MAY 20, 2005; ACCEPTED AUGUST 16, 2006;
ADVANCE ACCESS PUBLICATION SEPTEMBER 26, 2006

The Merensky Reef of the Bushveld Complex is one of the world's largest resources of platinum group elements (PGE); however, mechanisms for its formation remain poorly understood, and many contradictory theories have been proposed. We present precise compositional data [major elements, trace elements, and platinum group elements (PGE)] for 370 samples from four borehole core sections of the Merensky Reef in one area of the western Bushveld Complex. Trace element patterns (incompatible elements and rare earth elements) exhibit systematic variations, including small-scale cyclic changes indicative of the presence of cumulus crystals and intercumulus liquid derived from different magmas. Ratios of highly incompatible elements for the different sections are intermediate to those of the proposed parental magmas (Critical Zone and Main Zone types) that gave rise to the Bushveld Complex. Mingling, but not complete mixing of different magmas is suggested to have occurred during the formation of the Merensky Reef. The trace element patterns are indicative of transient associations between distinct magma layers. The porosity of the cumulates is shown to affect significantly the distribution of sulphides and PGE. A genetic link is made between the thickness of the Merensky pyroxenite, the total PGE and sulphide content, petrological and textural features, and the trace element signatures in the sections studied. The rare earth elements reveal the important role of plagioclase in the formation of the Merensky pyroxenite, and the distribution of sulphide.

KEY WORDS: *Merensky Reef; platinum group elements; trace elements*

INTRODUCTION

The Bushveld Complex (Fig. 1a and b) is the world's largest resource of platinum group elements (Pt, Pd, Ru, Rh, Os and Ir; referred to as PGE), located in three main occurrences—the Merensky Reef, UG-2 chromitite and Platreef. The UG-2 chromitite and the Merensky Reef are associated with a series of pyroxenite layers close in the stratigraphy to where ultramafic rocks of the Critical Zone give way to extensive development of norite in the Main Zone. This study focuses on the Merensky Reef in the western Bushveld Complex (Fig. 1c). Platreef mineralization is associated with the lower marginal contact in the northern limb of the Bushveld Complex. The Merensky pyroxenite is part of the Merensky Cyclic Unit and is located within the Upper Critical Zone of the Rustenburg Layered Suite (Fig. 1d).

The term 'Reef' refers to the economically important zone contained largely within a medium- to coarse-grained plagioclase-pyroxenite and is specifically the mining zone of payable metal values. The nature and location of the economic zone is highly variable both in thickness and in exact location (Viljoen & Hieber, 1986; Viljoen & Schurmann, 1998; Viljoen, 1999) and is usually, but not always, completely enclosed within the plagioclase-pyroxenite. Despite being mined for nearly 80 years, and the current focus of intense exploration and development, there is little consensus on the origin of the Merensky pyroxenite and the PGE mineralization.

*Corresponding author. Present address: School of Geosciences, The University of the Witwatersrand, Johannesburg, South Africa. Telephone: (27) 11 717 6547. Fax: (27) 11 717 6579. E-mail: wilsona@ukzn.ac.za

†Present address: Anglo American Platinum Corporation, P.O. Box 62179, Johannesburg, South Africa.

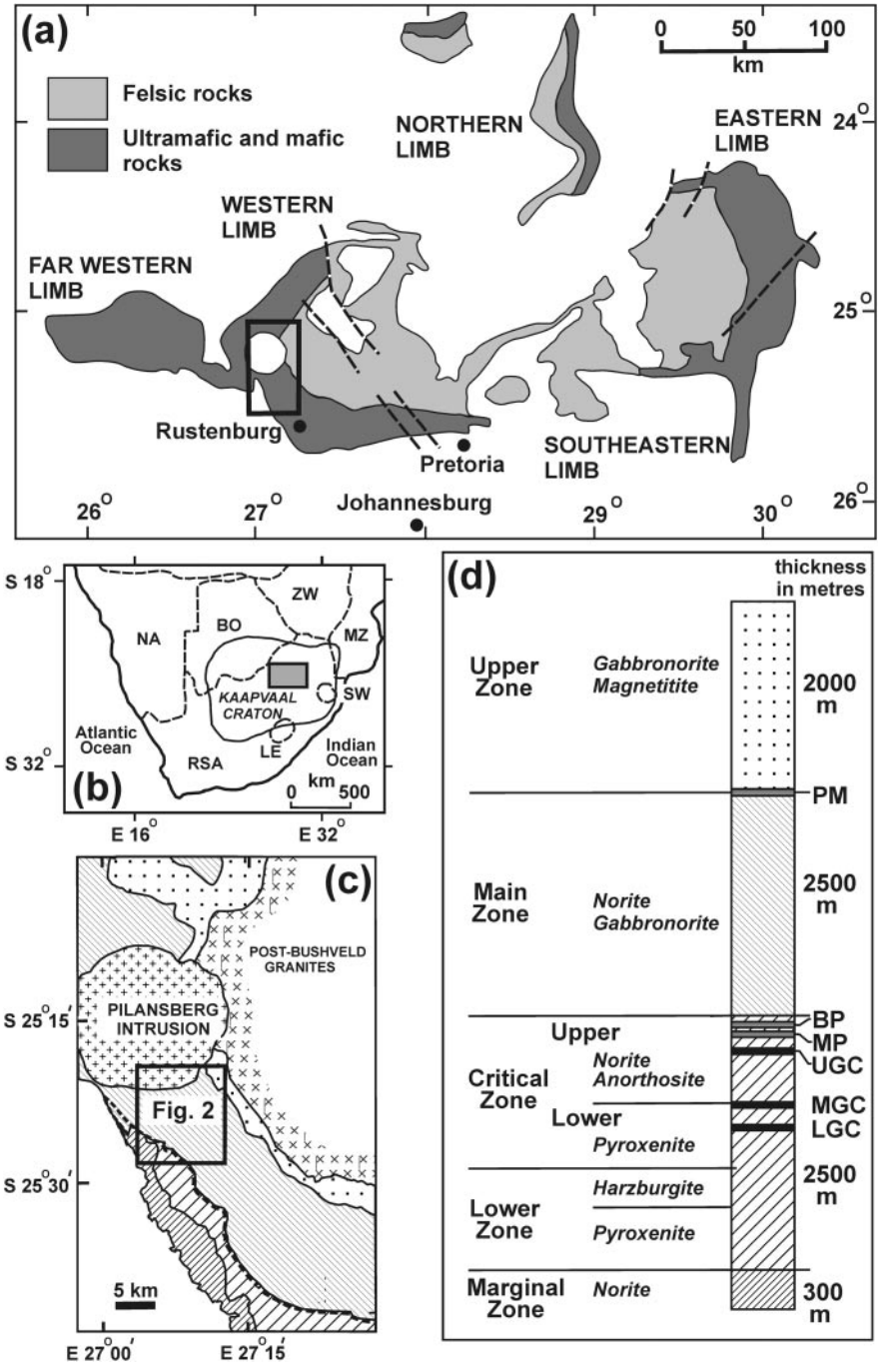

Fig. 1. (a) Geological map of the Bushveld Complex showing the area of interest (bold rectangle). (b) Location of Bushveld Complex in South Africa as shown in (a). (c) Simplified geological map of the western Bushveld Complex corresponding to rectangle in (a). (d) Simplified stratigraphy of the Bushveld Complex. PM, Pyroxenite Marker; BP, Bastard Pyroxenite; MP, Merensky Pyroxenite; UGC, Upper Group Chromitites; MGC, Middle Group Chromitites; LGC, Lower Group Chromitites. The section shown is called the Rustenburg Layered Suite. Ornamentations in (c) and (d) correspond to the same zones. The region in bold outline in (c) is the study area shown in Fig. 2.

The aim of this work is to examine the variability of the host Merensky pyroxenite in one area of the western Bushveld Complex where distinct facies changes occur, based on aspects of the textures, compositions, PGE and trace element contents of both the highly mineralized and less-mineralized portions of the pyroxenite.

Several important questions on the Merensky Reef remain to be answered. These include the link between

sulphide distribution and PGE mineralization in terms of the enclosing rock-types and silicate mineral associations, evidence for the possible involvement of hydrous fluids in the mineralization event, the extent to which fractional segregation of sulphide controlled the PGE distribution, and the role and nature of different magmas that may have interacted in this zone. The highly incompatible trace elements (Nb, Ta, Th, U, Zr, Hf) contained in the pyroxenite largely reflect the trapped liquid in the cumulates and, therefore, have the potential to provide important information on liquid compositions and the origin of the parent magmas. Apart from one specific type of narrow reef facies documented by Barnes & Maier (2002), there is scant information on the detailed distributions of these trace elements in the Merensky Reef, and none that consider a variety of reef types in a single area.

The limitation in most studies to date has been the restricted scope of the investigations, with few comparative data within local areas. Previous studies have focused on mine-wide occurrences of the Merensky Reef (Wilson *et al.*, 1999) or have been restricted to single borehole intersections (Barnes & Maier, 2002). In the present study, four borehole sections of undisturbed or 'normal' reef of contrasting types were investigated in one area in the western Bushveld Complex (Fig. 2). A total of 370 closely spaced samples were analysed, using high-precision analytical methods to determine major and trace element pattern types and the distribution of PGE.

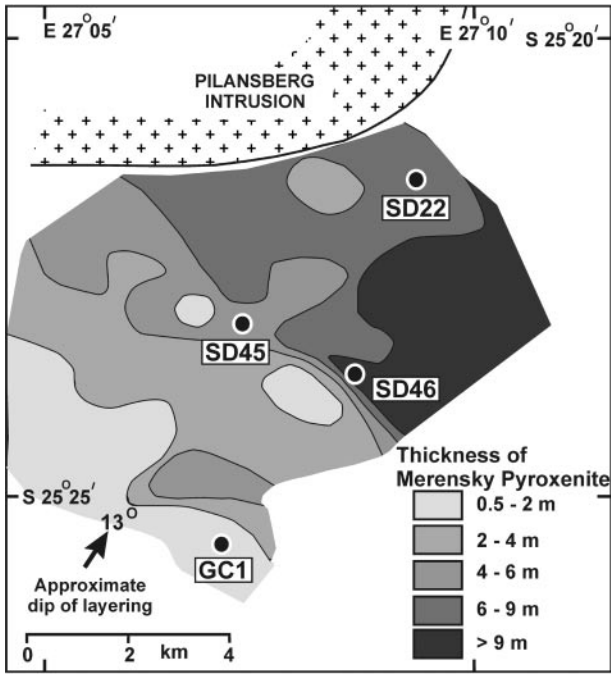

Fig. 2. Locations of the four drill cores that form the basis of this study and contoured thickness variation of the Merensky pyroxenite based on data from diamond drilling. Location of area shown in Fig. 1c.

THE BUSHVELD COMPLEX

Structure and stratigraphy

The Bushveld Complex is a large lopolithic intrusion of mafic and ultramafic cumulate rocks up to 10 km thick, formed from magmas that intruded the early Proterozoic Transvaal Supergroup at 2·05 Ga (Walraven *et al.*, 1990; Buick *et al.*, 2001). There are five main limbs of the intrusion developed on a regional basis (Fig. 1a) and each (possibly apart from the Far Western Limb) has essentially the same stratigraphic succession, comprising (from the base upwards) the Marginal, Lower, Critical, Main and Upper Zones. These make up the succession of mafic and ultramafic rocks called the Rustenburg Layered Suite (SACS, 1980). The Lower Zone and the lower part of the Critical Zone comprise ultramafic rocks (harzburgites and pyroxenite) and the Upper Critical Zone is made up of pyroxenite layers, norite and anorthosite. The Main and Upper Zones are norite and gabbronorite with magnetitite layers in the latter.

The Merensky Cyclic Unit, containing the Merensky pyroxenite, is located close to the boundary of the Upper Critical Zone and Main Zone. It is overlain by the Bastard Cyclic Unit, similar in form and thickness to the Merensky Cyclic Unit, but only sparsely mineralized. In general, the pyroxenite layer of the Merensky Cyclic Unit has a sharp lower contact, commonly with a narrow basal chromitite overlying pyroxene anorthosite, and an upper contact grading into norite. It ranges in thickness from 1 to 10 m and the mineralized zone varies in thickness from 10 to 200 cm. The PGE mineralization is associated with sulphide in the vicinity of, and generally overlying, one or more narrow chromitite layers, located approximately in the centre of the pyroxenite unit. These chromitites separate the pyroxenite into lower and upper portions. In some localities the economically important zone straddles the lower chromite layer and extends into the underlying norite. The texture is mainly cumulus orthopyroxene crystals enclosed within plagioclase with sparse large oikocrysts of clinopyroxene. Olivine is also present in some localities. In many occurrences parts of the lower pyroxenite may be pegmatoidal.

Terminology based strictly on modal mineral abundances (Le Maitre, 1989) classifies the 'pyroxenite' unit as a range of rock-types from true pyroxenite to melanorite; however, textures (relating mainly to the interstitial nature of the plagioclase) also need to be considered in the nomenclature (Gillespie & Styles, 1999; Brown, 2004). Recent classification of the Merensky pyroxenite based on whole-rock compositions, cumulus status of minerals and mineral proportions (Gillespie & Styles, 1999; Brown, 2004; Wilson *et al.*,

2005) recommended that these rocks be termed pyroxenite or plagioclase pyroxenite, depending on the amount of interstitial plagioclase present. In some sections, norite layers occur where plagioclase is cumulus; however, they are different from the footwall and hanging-wall norites, in which the plagioclase is strongly zoned.

Magma compositions of the Bushveld Complex

No chilled magma compositions that may represent the parental magmas to the Bushveld Complex have been found. Instead, different rock-types in the Marginal Zone and fine-grained sills in the sedimentary floor rocks have led to the recognition of several magma types (Cawthorn *et al.*, 1981; Sharpe, 1981; Davies & Tredoux, 1985; Harmer & Sharpe, 1985). However, it is debatable to what extent these rock compositions represent true liquids, are crystal-enriched liquids (Eales & Cawthorn, 1996), or indeed even reflect the range of Bushveld magmas (Eales & Cawthorn, 1996; Eales, 2002; Kruger, 2005). Ultramafic sills with spinifex pyroxene textures and quenched olivine are likely to represent closely the parent magmas (Davies *et al.*, 1980). The crystallization sequences of some of these reproduce that seen in the Bushveld Complex (Cawthorn & Davies, 1983). There is also evidence of considerable crustal assimilation (Cawthorn *et al.*, 1981). Compelling evidence for the emplacement of a different magma type that gave rise to the Main Zone compared with the Critical Zone is the marked overall, but erratic, increase in initial $^{87}Sr/^{86}Sr$ ratio close to the boundary of these rock units (Kruger, 1994). This change was initially shown to take place at the level of the Merensky pyroxenite (Kruger & Marsh, 1982) but subsequent studies have shown that no clear pattern exists (Lee & Butcher, 1990) and in some cases virtually no change in isotopic signature is observed at this level (Wilson *et al.*, 1999).

There is general acceptance that two main parental magmas gave rise to the Rustenburg Layered Suite (e.g. Eales, 2002). A high-magnesium andesite magma (somewhat akin to a boninite on major element grounds but lacking distinctive trace element characteristics), termed magma-type B1, gave rise to the Lower Zone and lower Critical Zones. Low-magnesium, low-Ti-tholeiitic basalts, termed magma-types B2 and B3, were the principal components of the Main Zone and Upper Zone (Sharpe, 1981; Irvine & Sharpe, 1983; Harmer & Sharpe, 1985; Sharpe & Hulbert, 1985; Curl, 2001). There is no agreement on the precise compositions of these proposed parental magmas (Eales & Cawthorn, 1996; Eales, 2002), and Kruger (2005) provided interpretative evidence to suggest that up to five distinct magma types were involved in the formation of the Rustenburg Layered Suite. Therefore, the two broad magma types that gave rise to the Critical Zone and Main Zone will be referred to in this study in more general terms as Critical Zone (CZ) and Main Zone (MZ) magmas, respectively.

The CZ and MZ parental magmas are differentiates of more primitive magmas with relatively steep rare earth element (REE; normalized La/Yb = 5–12) patterns and with Nd isotope characteristics indicative of crustal contamination with a change in εNd (t = 2·05 Ga) from +5·5 to +7·0. This change occurs in the transition zone from the Upper Critical Zone to the Main Zone at the approximate level of the Merensky Reef (Maier *et al.*, 2000). The Re–Os isotopic compositions of the Merensky Reef sulphides (Schoenberg *et al.*, 1999) are highly radiogenic and also highly variable ($^{187}Os/^{188}Os$ 0·168–0·181), further confirming a continental crustal signature. The CZ magma has a higher concentration of incompatible trace elements and a steeper REE pattern than the MZ magma.

An important feature of the Bushveld Complex is that PGE are present in variable but low levels (10–200 ppb) in most rocks (including chromitites and pyroxenite) of the Lower Zone and Lower Critical Zone, and it is likely that the parental magma that gave rise to these rocks was also relatively enriched in PGE (Lee, 1996). Recent estimates of the Pd content of the CZ magma are as high as 100 ppb (R. Keays, personal communication, 2005).

Precise trace element data for the most primitive magma compositions of the Bushveld Complex remain sparse. X-ray fluorescence (XRF) data have been obtained for marginal sills that occur in the country rock peripheral to both the eastern and western Bushveld Complex (Davies *et al.*, 1980; Cawthorn *et al.*, 1981). A recent study (Curl, 2001) reported precise trace element data for marginal sills in the eastern Bushveld Complex, of both quenched and fine-grained granular varieties, and these data are used in this study for comparative purposes. Two broad compositional types of sills were identified corresponding to B1 (or Critical Zone-type) and B2/B3 (or Main Zone-type) magmas.

GEOLOGICAL SETTING OF THE STUDY AREA

The Merensky Reef sequence is highly variable throughout the Bushveld Complex, both in thickness and lithology. Within the area of interest there is a recognizable facies change that includes significant variation in thickness of the Merensky pyroxenite (Fig. 2). The economic zone (the Merensky Reef) is identified by the development of abundant (2–5 vol. %), net textured to disseminated sulphide comprising pyrrhotite, pentlandite and chalcopyrite. This zone is typically about 1 m thick but lesser amounts of mineralization are developed above and below the economic zone.

The objective of this study is to investigate the Merensky Reef in a localized area encompassing a variety of undisturbed reef types (as opposed to disturbed pothole reef), where thickness of the pyroxenite is observed to vary. Four drill cores (GC1, SD45, SD22 and SD46) through the sequence were selected for detailed study (Fig. 2). In drill hole SD22, two deflections (two sub-parallel drill cores branching off the mother hole at depth) designated D3 and D5, separated spatially by about 1·5 m at 1500 m depth, were analysed for trace elements to investigate short range differences. The cores were logged to establish lithologies and textural types.

The four sections cover a lateral distance of about 5 km and range from the narrow Rustenburg-type 'thin-reef' facies (Wilson *et al.*, 1999) of GC1 to thick-reef types (also colloquially called 'Swartklip facies' type; Viljoen & Schurmann, 1998) of SD22 and SD46. In GC1 the pyroxenite and the associated mineralization occur over a narrow vertical interval of 60 cm compared with SD46 where the pyroxenite is 10 m thick. A geographically restricted zone characterized by an intermediate facies separates these two distinct types and is represented by SD45. The position of GC1 is closer to the margin of the RLS, whereas the intermediate and thick-reef types are progressively further from the margin.

SAMPLING AND ANALYSIS

A major limitation in studies of the Merensky Reef to date has been the selected nature of the samples and the variable types of data because of the different sampling and analytical techniques used. In this study an attempt is made to compare an internally consistent dataset for samples that have been prepared and analysed in the same manner. A problem with sampling the Merensky Reef using drill core intersections has been the extent to which the samples are sufficiently representative of the vertical interval to elucidate small-scale variations (Wilson *et al.*, 1999). In this study, wide diameter whole-core samples 60 mm in diameter (as opposed to commonly used half or quarter core) were sampled at between 5 and 10 cm intervals depending on the thickness of the pyroxenite unit. The narrow-type facies (GC1) was drilled to yield core 105 mm in diameter allowing the pyroxenite to be sampled over 1 cm intervals, each sample yielding about 100 g of rock. All cores were sampled on a continuous basis between the footwall of the Merensky pyroxenite into the norite hanging wall, giving a total number of 370 samples.

Trace element and PGE concentrations were determined by inductively coupled plasma mass spectrometry (ICP-MS) on separate whole-rock fractions derived from the same sample using an Elan Sciex® 6100 system. High-temperature (260°C)–high-pressure (75 bars) dissolution in $HF–HNO_3$ was essential to dissolve the highly refractory mineral constituents that largely control the incompatible trace element budget. Closed Teflon® beaker dissolutions yielded erratic data 5–50% lower than the high-pressure dissolution method, because of the inability to dissolve refractory minor mineral components such as zircon, badelleyite and zirconolite. After drying down, the final dissolution was made up to 50 ml in 10% nitric acid that also contained the internal standards Rh, In, Re and Bi (a correction was made for those ore samples that contained Rh). Analysis was carried out against certified standard solutions from Specpure® and Perkin Elmer®. PGE pre-concentration was by means of the standard Ni–S fire assay method and the analysis was completed by ICP-MS. A further factor that was studied was the influence of particle size in the milled material and sample homogenization. It was ascertained that reproducible results for trace elements determined by ICP-MS could not be obtained on sample material where the median grain size exceeded 20 μm. In this exercise, samples were milled to <20 μm, with the median close to 10 μm. Milling was carried out using a high-purity C-steel swing mill. Size distributions were determined using a Malvern laser particle analyser.

Calibrations were against certified analytical solutions and international certified reference materials (BHVO-1, BCR-1 and BR-1), which were analysed with every run. All samples were analysed in duplicate. A further laboratory control (SD22 4691) was analysed with every sample batch. International reference materials SARM6 and SARM7 were analysed to ensure the accuracy of the PGE data. The accuracy and precision of the trace element data were typically about 5%. Detection limits for incompatible elements were determined using high-purity olivine separates (Fo_{94}) from the Great Dyke which for Nb and Ta were both <1 ppb. Detection limits for PGE were better than 2 ppb for all elements. Whole-rock element analyses were carried out on fusion discs using a Philips PW1404 XRF spectrometer. S was determined by XRF using pressed pellets and matrix-matched standards, and a Cr-target X-ray tube.

Total Fe was analysed and Fe^{3+}/Fe^{2+} was calculated on the basis of 10% Fe^{3+} of total Fe. Normative minerals were calculated using the standard method (Johannsen, 1931). Plagioclase components were grouped together and normative En, Fs and Wo components were combined to give diopside and orthopyroxene components.

Analyses of selected samples from all drill cores representing the range of major and trace element contents are given in Table 1. The complete dataset used in the study is given in the Electronic Appendix (http://www.petrology.oxfordjournals.org).

Table 1: Representative analyses of samples from the four drill cores studied

Drill core:	GC1	GC1	GC1	GC1	GC1	GC1	SD22 D5	SD22 D5	SD22 D5
Sample:	9	26	34	39	47	55	4682	4693	4704
From (m):	56·080	57·080	57·389	57·470	57·599	57·753	1464·35	1465·49	1466·66
Interval (m):	0·060	0·060	0·016	0·016	0·019	0·060	0·101	0·103	0·095
Major elements as oxides (wt %)									
SiO_2	53·27	53·04	52·54	52·02	49·97	47·8	53·42	53·55	53·13
Al_2O_3	5·37	5·51	5·52	9·77	8·06	28·12	5·75	6·14	5·89
Fe_2O_3*	1·35	1·29	1·31	1·05	1·38	0·32	1·22	1·22	1·2
FeO	10·91	10·38	10·55	8·5	11·17	2·62	9·87	9·89	9·75
MnO	0·25	0·23	0·24	0·2	0·22	0·04	0·22	0·23	0·22
MgO	22·58	23·36	23·5	20·3	20·04	2·94	23·40	23·56	23·77
CaO	4·96	4·64	4·53	5·83	4·75	14·77	4·71	4·41	4·77
Na_2O	0·51	0·55	0·42	0·87	0·77	2·09	0·65	0·47	0·42
K_2O	0·05	0·04	0·04	0·07	0·12	0·15	0·08	0·07	0·02
TiO_2	0·22	0·2	0·18	0·14	0·34	0·05	0·20	0·19	0·16
P_2O_5	0·04	0·02	0·02	0·0	0·01	0·0	0·03	0·03	0·01
Cr_2O_3	0·35	0·34	0·62	0·98	2·24	0·06	0·40	0·38	0·41
NiO	0·15	0·32	0·20	0·10	0·25	0·30	0·18	0·09	0·11
Total†	99·98	99·89	99·64	99·82	99·32	99·24	100·10	100·20	99·86
Trace elements (ppm)									
V	115	110	116	113	232	23	109	105	109
Cr	1868	1906	4427	8939	12403	387	2307	2048	2376
Co	100	126	109	85	102	50	98	87	91
Ni	1152	2631	1658	767	1703	2373	1295	686	772
Cu	298	970	565	213	900	1054	458	112	185
S	4024	10847	5438	863	6101	7684	4095	1170	1401
Zn	70	53	53	51	94	20	61	61	60
Rb	0·8	0·4	0·6	1	3	1·1	2·8	2	0·6
Sr	57	63	63	117	92	330	59	63	65
Zr	7·7	8·4	6·1	5·2	10·5	1·7	8·9	6·8	3·3
Nb	0·254	0·223	0·169	0·207	0·557	0·044	0·341	0·263	0·061
La	1·719	1·953	1·02	0·989	1·516	1·888	1·393	1·633	0·738
Ce	4·199	4·426	2·515	2·045	3·259	3·44	3·088	3·421	1·362
Pr	0·588	0·547	0·325	0·243	0·422	0·37	0·412	0·408	0·193
Nd	2·706	2·278	1·459	0·99	1·737	1·282	1·812	1·600	0·844
Sm	0·688	0·563	0·392	0·242	0·421	0·253	0·467	0·394	0·228
Eu	0·148	0·144	0·116	0·146	0·159	0·293	0·134	0·139	0·12
Gd	0·767	0·646	0·472	0·288	0·482	0·246	0·548	0·463	0·284
Tb	0·14	0·114	0·093	0·051	0·085	0·032	0·104	0·082	0·058
Dy	0·944	0·751	0·633	0·353	0·614	0·17	0·719	0·567	0·438
Ho	0·212	0·164	0·148	0·082	0·139	0·033	0·163	0·132	0·105
Er	0·634	0·482	0·444	0·262	0·413	0·094	0·482	0·402	0·316
Tm	0·106	0·080	0·077	0·044	0·072	0·014	0·084	0·070	0·058
Yb	0·703	0·526	0·512	0·316	0·477	0·09	0·560	0·482	0·388
Lu	0·113	0·083	0·082	0·052	0·079	0·013	0·092	0·080	0·065
Hf	0·249	0·271	0·202	0·155	0·318	0·058	0·292	0·228	0·133
Ta	0·016	0·015	0·01	0·012	0·037	0·001	0·023	0·019	0·004
Th	0·147	0·117	0·091	0·105	0·349	0·015	0·263	0·156	0·041
U	0·048	0·053	0·036	0·029	0·091	0·007	0·066	0·055	0·013

Drill core:	GC1	GC1	GC1	GC1	GC1	GC1	SD22 D5	SD22 D5	SD22 D5
Sample:	9	26	34	39	47	55	4682	4693	4704
From (m):	56·080	57·080	57·389	57·470	57·599	57·753	1464·35	1465·49	1466·66
Interval (m):	0·060	0·060	0·016	0·016	0·019	0·060	0·101	0·103	0·095
Platinum group elements and Au (ppb)									
Au	47	140	315	43	2113	524	n.d.	n.d.	n.d.
Ir	3	14	76	21	172	67	n.d.	n.d.	n.d.
Os	2	14	58	15	134	59	n.d.	n.d.	n.d.
Pd	28	316	1275	116	1686	2312	n.d.	n.d.	n.d.
Pt	66	944	4080	605	4834	3922	n.d.	n.d.	n.d.
Rh	4	30	225	53	554	203	n.d.	n.d.	n.d.
Ru	16	82	408	132	1003	394	n.d.	n.d.	n.d.

Drill core:	SD22 D5	SD22 D5	SD45	SD45	SD45	SD45	SD45	SD46	SD46
Sample:	4710	4743	23	30	46	59	65	1	11
From (m):	1467·19	1470·60	811·47	811·80	812·61	813·27	813·57	883·50	884·52
Interval (m):	0·105	0·100	0·04	0·05	0·06	0·05	0·06	0·10	0·10
Major elements as oxides (wt %)									
SiO_2	52·62	48·29	43·67	53·44	47·48	46·31	44·73	53·16	54·24
Al_2O_3	4·99	31·78	4·33	4·19	5·07	10·59	11·24	11·54	6·18
Fe_2O_3*	1·46	0·09	1·89	1·42	1·55	1·34	1·44	0·94	1·19
FeO	11·78	0·76	15·33	11·52	12·51	10·78	11·59	7·58	9·58
MnO	0·25	0·01	0·27	0·24	0·21	0·2	0·19	0·16	0·22
MgO	22·41	0·71	22·09	23·38	28·49	23·44	23·12	17·37	22·80
CaO	5·13	15·86	2·31	3·06	3·02	6·28	5·74	7·32	4·07
Na_2O	0·51	2·49	0·25	0·56	0·19	0·47	0·73	1·03	0·67
K_2O	0·16	0·13	0·02	0·48	0·09	0·09	0·11	0·22	0·33
TiO_2	0·27	0·03	0·77	0·32	0·17	0·15	0·10	0·17	0·23
P_2O_5	0·02	0·02	0·01	0·01	0·06	0·03	0·01	0·01	0·01
Cr_2O_3	0·46	0·02	5·93	0·46	0·55	0·15	0·31	0·30	0·36
NiO	0·14	0·00	0·42	0·4	0·25	0·22	0·42	0·11	0·14
Total†	100·20	100·19	97·26	99·47	99·61	100·02	99·71	99·88	99·99
Trace elements (ppm)									
V	122	10	771	125	81	42	42	93	100
Cr	2539	17	43625	2464	3436	975	2000	912	2282
Co	95	4	186	134	145	135	165	39	101
Ni	1008	18	3356	2950	1947	1660	3074	904	1111
Cu	206	6	1481	822	206	96	1095	267	300
S	1877	10	10519	7319	1669	754	6129	2071	2701
Zn	81	18	212	78	69	59	67	48	59
Rb	6·1	1·6	1·3	16·6	3·8	3·7	3·1	7·6	11·3
Sr	58	400	43	45	58	166	153	142	77
Zr	11·1	1·2	6·9	13·6	10·8	16·1	9·1	13·3	22·1
Nb	0·535	0·058	0·42	2·576	0·73	1·214	0·596	0·904	1·344
La	2·086	1·300	1·158	3·577	2·943	4·171	2·039	2·297	4·68
Ce	5·167	2·208	2·426	8·141	6·465	8·49	3·997	4·758	8·274
Pr	0·815	0·243	0·31	0·938	0·701	0·978	0·46	0·587	0·887
Nd	3·964	0·826	1·314	3·519	2·453	3·608	1·666	2·249	2·967
Sm	1·044	0·157	0·341	0·823	0·472	0·717	0·342	0·522	0·658
Eu	0·295	0·288	0·094	0·190	0·123	0·275	0·184	0·233	0·190

Table 1: *Continued*

Drill core:	SD22 D5	SD22 D5	SD45	SD45	SD45	SD45	SD45	SD46	SD46
Sample:	4710	4743	23	30	46	59	65	1	11
From (m):	1467·19	1470·60	811·47	811·80	812·61	813·27	813·57	883·50	884·52
Interval (m):	0·105	0·100	0·04	0·05	0·06	0·05	0·06	0·10	0·10
Gd	1·147	0·140	0·416	0·876	0·547	0·757	0·375	0·597	0·798
Tb	0·215	0·017	0·081	0·143	0·073	0·105	0·052	0·1	0·116
Dy	1·423	0·087	0·602	0·947	0·442	0·589	0·31	0·669	0·741
Ho	0·311	0·017	0·146	0·212	0·094	0·119	0·068	0·148	0·162
Er	0·893	0·043	0·454	0·628	0·277	0·334	0·189	0·445	0·474
Tm	0·145	0·007	0·082	0·108	0·043	0·051	0·031	0·076	0·079
Yb	0·954	0·037	0·569	0·728	0·302	0·329	0·207	0·507	0·522
Lu	0·152	0·005	0·094	0·121	0·049	0·052	0·034	0·081	0·085
Hf	0·417	0·032	0·253	0·52	0·317	0·453	0·249	0·401	0·630
Ta	0·038	0·003	0·022	0·162	0·049	0·077	0·038	0·076	0·095
Th	0·285	0·032	0·139	1·501	0·365	0·800	0·346	0·898	1·109
U	0·129	0·012	0·042	0·569	0·114	0·206	0·103	0·203	0·487
Platinum group elements and Au (ppb)									
Au	n.d.	n.d.	277	226	52	32	761	36	57
Ir	n.d.	n.d.	102	164	13	12	84	d.l.	3
Os	n.d.	n.d.	71	116	11	10	64	d.l.	d.l.
Pd	n.d.	n.d.	907	3422	350	180	2223	14	23
Pt	n.d.	n.d.	4332	10357	1285	374	4651	43	61
Rh	n.d.	n.d.	287	492	41	40	283	2	4
Ru	n.d.	n.d.	512	880	74	72	444	3	12

Drill core:	SD46	SD46	SD46	SD46	SD46
Sample:	13	30	40	50	78
From (m):	884·72	886·37	887·37	888·37	891·22
Interval (m):	0·10	0·10	0·10	0·10	0·10
Major elements as oxides (wt %)					
SiO_2	53·80	50·39	54·71	53·29	53·95
Al_2O_3	6·24	9·09	3·94	6·81	5·29
Fe_2O_3*	1·16	1·10	1·23	1·12	1·21
FeO	9·38	8·91	9·91	9·08	9·78
MnO	0·22	0·19	0·23	0·21	0·23
MgO	22·43	23·45	23·34	23·60	23·55
CaO	4·47	5·30	3·97	4·62	4·35
Na_2O	0·78	0·77	0·60	0·69	0·68
K_2O	0·33	0·10	0·67	0·08	0·24
TiO_2	0·24	0·12	0·39	0·17	0·27
P_2O_5	0·20	0·01	0·11	0·00	0·04
Cr_2O_3	0·36	0·35	0·40	0·39	0·38
NiO	0·10	0·14	0·09	0·08	0·08
Total†	99·70	99·90	99·57	100·12	100·03
Trace elements (ppm)					
V	98	61	123	89	117
Cr	2055	2010	2009	2063	2111
Co	89	104	91	93	92

Drill core:	SD46	SD46	SD46	SD46	SD46
Sample:	13	30	40	50	78
From (m):	884·72	886·37	887·37	888·37	891·22
Interval (m):	0·10	0·10	0·10	0·10	0·10
Ni	838	1015	677	655	642
Cu	171	76	38	42	27
S	1505	531	261	308	226
Zn	59	54	74	68	75
Rb	10·3	2·5	25·7	1·6	7·1
Sr	84	120	41	101	76
Zr	18·8	8·5	37·2	7·5	18·3
Nb	1·65	0·472	3·667	0·283	1·152
La	10·211	1·729	7·516	1·877	4·507
Ce	21·251	3·383	17·823	3·504	9·565
Pr	2·548	0·385	2·232	0·417	1·157
Nd	9·088	1·403	8·422	1·621	4·448
Sm	1·636	0·302	1·635	0·378	0·930
Eu	0·279	0·148	0·262	0·176	0·243
Gd	1·859	0·332	1·761	0·435	1·007
Tb	0·219	0·05	0·243	0·075	0·155
Dy	1·147	0·312	1·385	0·495	0·921
Ho	0·225	0·069	0·281	0·11	0·196
Er	0·639	0·204	0·79	0·329	0·554
Tm	0·091	0·034	0·119	0·055	0·088
Yb	0·586	0·233	0·76	0·365	0·569
Lu	0·089	0·038	0·119	0·059	0·089
Hf	0·544	0·247	1·152	0·239	0·539
Ta	0·108	0·028	0·24	0·019	0·074
Th	1·206	0·263	2·48	0·158	0·687
U	0·416	0·085	0·478	0·061	0·211
Platinum group elements and Au (ppb)					
Au	28	30	9	7	d.l.
Ir	d.l.	7	d.l.	d.l.	d.l.
Os	d.l.	7	d.l.	d.l.	d.l.
Pd	15	189	19	25	2
Pt	35	401	19	57	7
Rh	3	23	2	3	d.l.
Ru	7	35	3	5	d.l.

*Fe_2O_3 assigned on the basis of 10 wt % Fe.
†Total anhydrous.
Detection limits (d.l.) (ppb): Au 2, Ir 1, Os 1, Pd 2, Pt 1, Rh 1, Ru 1. n.d., not determined.

ROCK-TYPES, TEXTURES AND MAJOR ELEMENT COMPOSITIONS

Rock-types

The Merensky Reef exhibits considerable variation petrographically and texturally; detailed descriptions have been given for several sections in the eastern (Seabrook *et al.*, 2005) and western Bushveld Complex (Leeb-du Toit, 1986; Wilson *et al.*, 1999; Barnes & Maier, 2002). Different descriptive techniques and analytical strategies allow only limited correlation between these studies. The rock-types observed in cores SD45, SD46, GC1 and SD22, from base to top, are as follows (Fig. 3): leuconorite or pyroxene anorthosite footwall; a narrow basal chromitite (BC) 2–10 mm thick with sharp contacts; lower pyroxenite unit, which on the basis

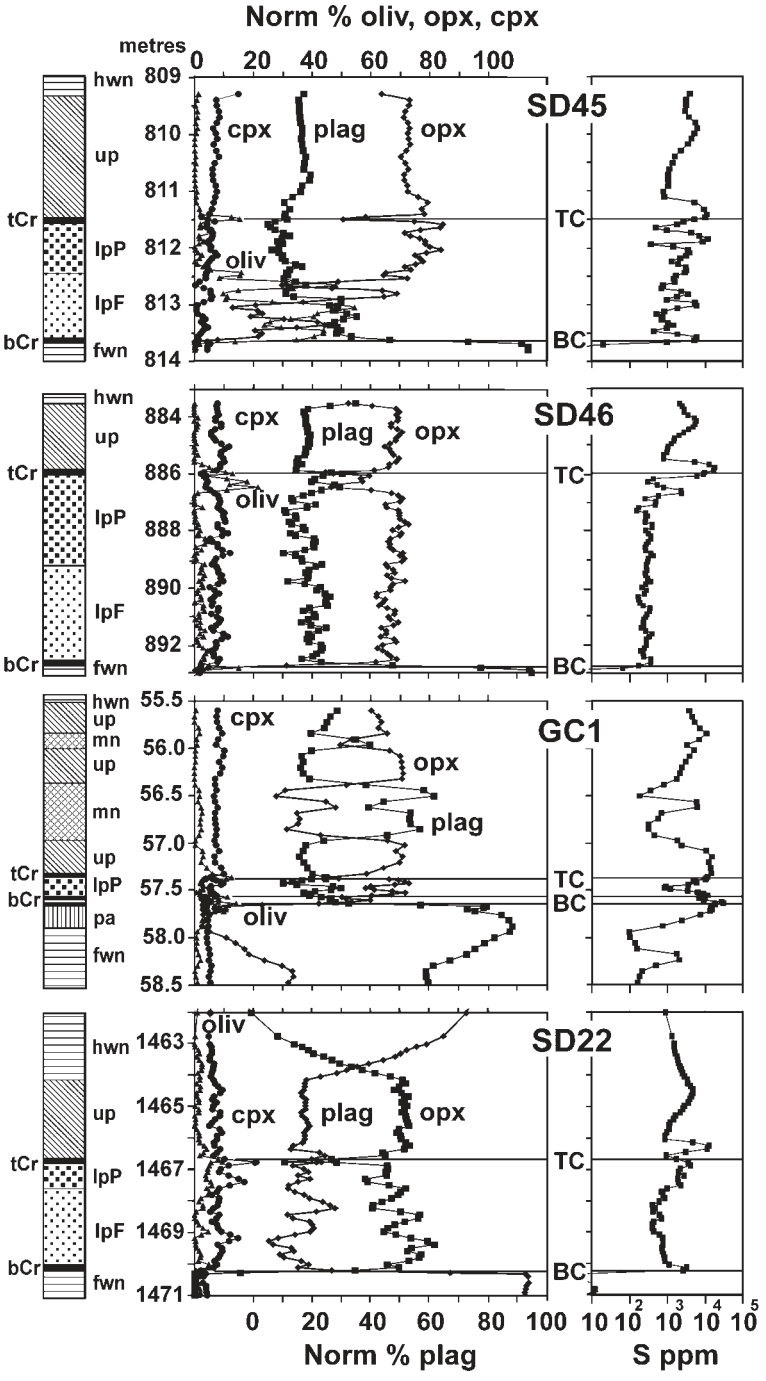

Fig. 3. Rock-types, normative (CIPW) mineralogy and bulk-rock S content in the four drill cores intersecting the Merensky pyroxenite. hwn, hanging-wall norite; up, upper pyroxenite; tCr, top chromitite; bCr, bottom chromitite; lpP, lower pegmatoidal plagioclase-pyroxenite; lpF, lower plagioclase-pyroxenite; pa, pyroxene-anorthosite; mn, melanorite; fwn, footwall norite. Modal mineralogy variation is prefixed by the normative mineral; olivine (oliv), orthopyroxene (opx), clinopyroxene (cpx) and plagioclase (plag). The positions of the topmost chromitite (TC) and bottom chromitite (BC) are shown. Depths are shown relative to borehole surface collars.

of its modal mineralogy ranges from pyroxenite and olivine pyroxenite to plagioclase pyroxenite; narrow top chromitite (TC); upper plagioclase pyroxenite; hanging-wall norite with gradational contact. The upper portions of the lower pyroxenite are commonly pegmatoidal.

In the Merensky pyroxenite, orthopyroxene as a cumulus phase is the most abundant mineral, followed

by plagioclase with minor clinopyroxene. The crystal size of the clinopyroxene is highly variable, ranging from 2 to 20 mm. Plagioclase occurs as large optically continuous oikocrysts 20–60 mm in diameter that enclose orthopyroxene. These oikocrysts commonly have an unzoned core and are strongly zoned towards the margins. In some cases, small (1–2 mm), strongly compositionally zoned plagioclase laths as cumulus crystals are present in specific layers. In the footwall and hanging-wall norite, plagioclase occurs as well-developed laths with minor compositional zoning. Olivine occurs in some sections as cumulus, oikocrystic, or skeletal crystals, or in reaction relationship with orthopyroxene.

Major element compositions and sulphide distributions

Because of the relatively coarse-grained nature of the pyroxenite, modal mineralogy estimates based on whole-rock normative compositions most readily represent the mineralogical variations in the four sections (Fig. 3). Figure 3 also shows the variation of S concentration, which reflects the distribution of sulphide. In all sections the lower pyroxenite unit exhibits pronounced small-scale mineralogical variations whereas the upper pyroxenite is relatively homogeneous. The distribution of normative orthopyroxene content is opposite to that of plagioclase. Variation in the lower pyroxenite is more marked in the transitional (SD45) and marginal (GC1) reef types. The thin facies-type GC1 has a series of pyroxenite and norite layers above the upper pyroxenite.

The distribution of sulphide (Fig. 3) is broadly similar in the transitional (SD45) and thick-reef sections (SD22 and SD46). There is a marked increase in S content at the base of the lower pyroxenite to relatively low levels of 100–1000 ppm S. A small S peak generally occurs immediately above the basal chromitite (BC). Small-scale variations are present, which in most cases coincide with increases in orthopyroxene. At the top of the lower pyroxenite, S content increases markedly through a series of well-defined layers. In all cases the highest S peak is located immediately above the top chromitite (TC). In the thin reef-type (GC1) S distribution is markedly different from the thicker reef-types. The thin pyroxenite of this facies-type cannot be clearly divided into a lower and upper pyroxenite. S attains relatively high concentrations in the norite below the BC and rises to a maximum to coincide with this chromitite. There is a marked decrease of S content in the centre of the pyroxenite, rising again higher in the unit.

Textural associations

Drill core SD22 illustrates the ranges of textures observed in the pyroxenite unit (Fig. 4). These textures relate mainly to the association of orthopyroxene and plagioclase, with orthopyroxene occurring as coarse-grained, irregular-shaped crystals with interstitial, or irregular-shaped plagioclase laths (Fig. 4a–d), to varieties with elongate orthopyroxene (Fig. 4e and f), and close-packed orthopyroxene (Figs. 4g and h). Part of SD45 (Fig. 4i) is a very coarse-grained (pegmatoidal) olivine pyroxenite with 'harrisitic' textures in which olivine (and more rarely orthopyroxene) occurs as elongate, hollow and hooked-shaped grains. These textures are typical of crystals that have grown rapidly in a high thermal gradient (Donaldson, 1974). Sulphide consists of an intergrowth of pyrrhotite (40–50%), pentlandite (20–40%), and chalcopyrite (15–25%). There commonly exists a well-developed zonal relationship, with the chalcopyrite forming the outer rim to the Fe–Ni sulphides.

Small pockets of primary hydrous phases (phlogopite and amphibole) (Fig. 4c and d), and magnetite, are locally developed together with alteration of the primary silicates (fibrous amphibole). These pockets commonly include late-stage accessory phases such as zircon, badelleyite, apatite, zirconolite, rutile and davidite as extremely small crystals (Ohnenstetter *et al.*, 1998). These mineral associations are interpreted as resulting from the concentration of late-stage (hydrous) fluids as the last vestiges of the solidification process. There is no evidence of segregation or settling of dense minerals that could have caused decoupling of trace elements.

TRACE ELEMENT COMPOSITIONS

Distributions of incompatible trace elements in the Merensky Reef

Ratios of incompatible trace elements provide a broad basis for establishing a link between the mafic cumulates and possible parental magmas. Ratios involving Nb, Th, U and La (Fig. 5a and b) delineate distinct fields for the two broad magma types recognized in the marginal sills and considered to be representative of Bushveld parental magmas. Ratios for different pyroxenites of the Merensky unit overlap, but are largely intermediate between the main magma-type fields, plausibly supporting mixing or mingling (a situation where mixing is incomplete) of the two magmas. There is also correspondence between the plagioclase content (expressed as normative wt %) and incompatible element ratios. However, the relationship is not linear for all samples in the pyroxenite section, but rather defines a series of sub-parallel arrays for sets of contiguous samples (shown for SD22 in Fig. 5c). The arrays, therefore, define narrow intervals in the sequence where variations in Th/Nb show inherent changes with normative plagioclase content. Values of Th/Nb for the Merensky pyroxenites are intermediate between the two inferred parent magma compositions, but there is also a tendency

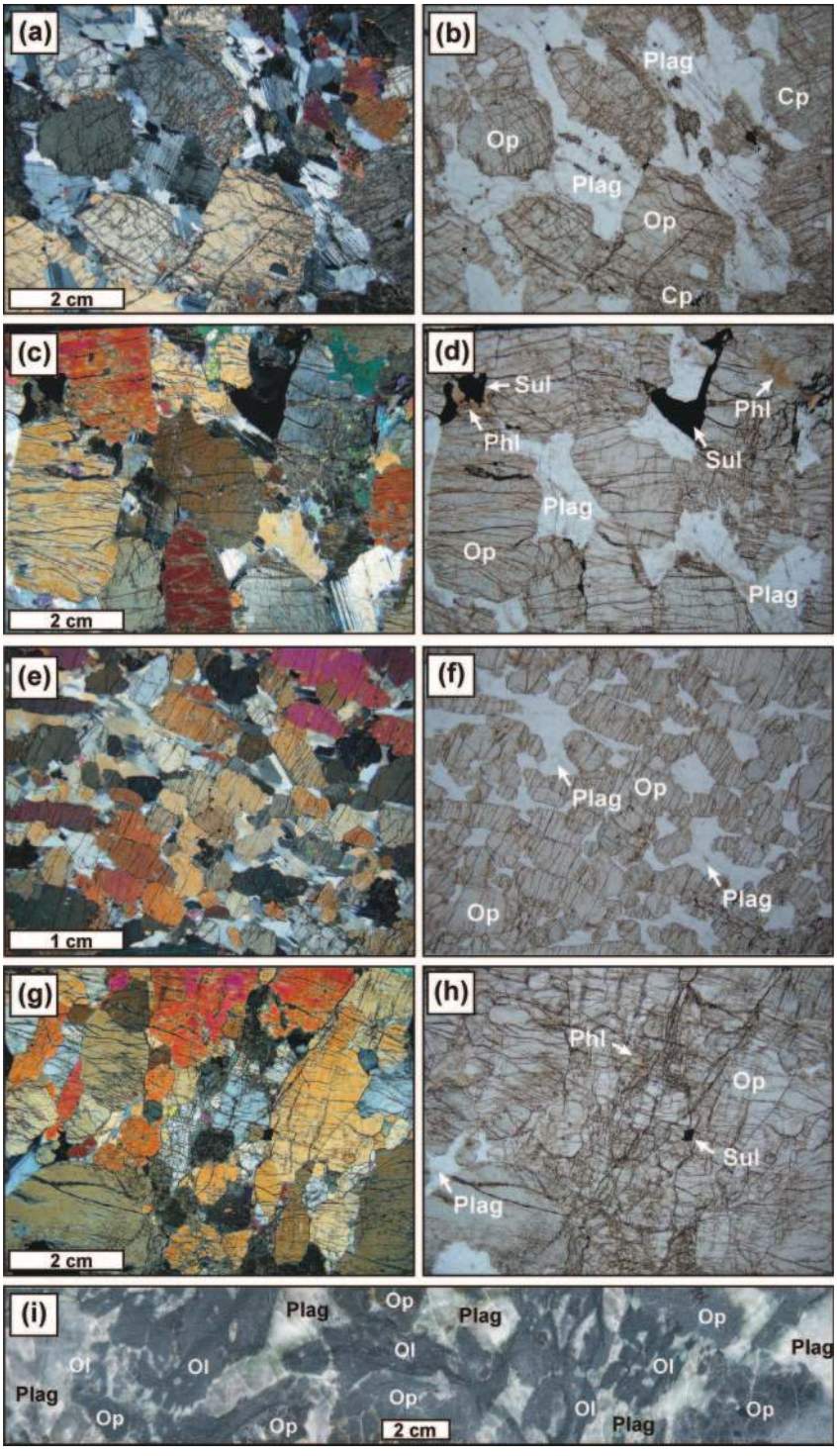

Fig. 4. Petrographic characteristics of the Merensky pyroxenite. Op, orthopyroxene; Cp, clinopyroxene; Plag, plagioclase; Sul, sulphide; Phl, phlogopite. (a) SD22 D5 upper pyroxenite sample 4776 at 1463·71 m. Coarse-grained orthopyroxene, rare crystals of clinopyroxene and interstitial laths of strongly zoned plagioclase. (b) Same as previous view under partly crossed polars. (c) SD22 D5 upper pyroxenite sample 4684 at 1464·55 m. Coarse-grained orthopyroxene enclosed within optically continuous interstitial plagioclase. Sulphide and phlogopite are also interstitial. (d) Same as previous view under partly crossed polars. (e) SD22 D5 lower pyroxenite sample 4720 at 1468·23 m. Fine-grained elongate laths of cumulus orthopyroxene enclosed within interstitial plagioclase. (Note change in scale.) (f) Previous view under partly crossed polars. (g) SD22 D5 sample 4731 at 1469·49 m. Close-packed and elongate orthopyroxene with interstitial plagioclase. (h) Same as previous view under partly crossed polars. (i) Polished core section SD45 at 812·3 m showing pegmatoidal texture and harrisitic development of olivine.

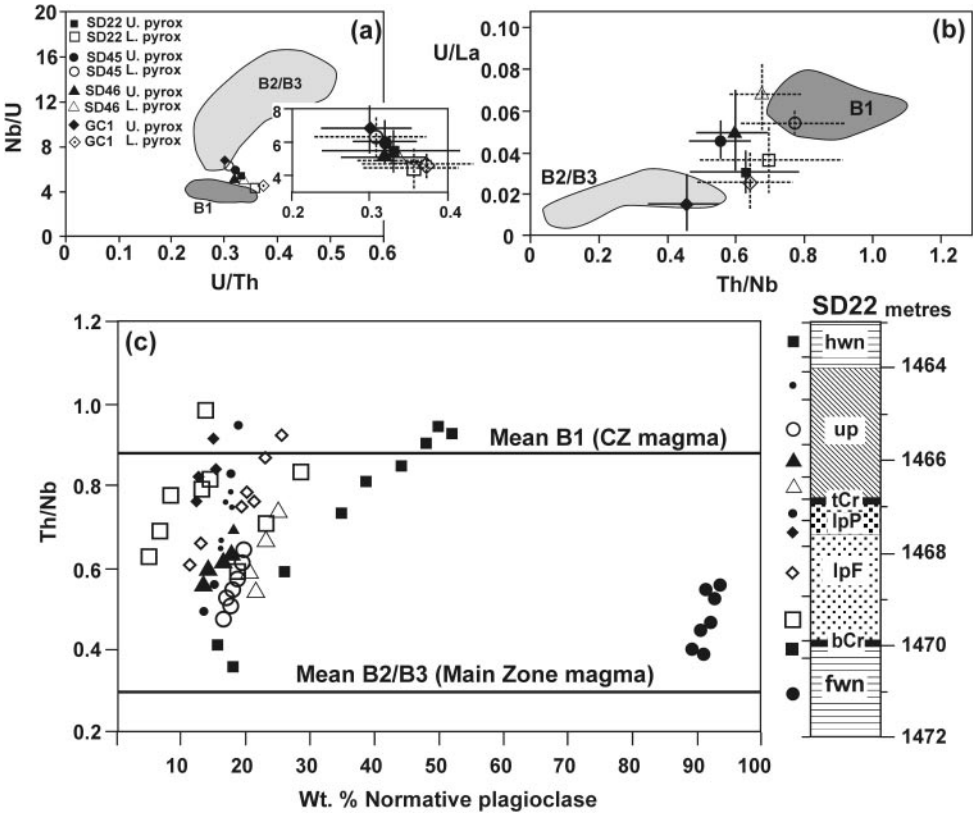

Fig. 5. Incompatible trace element ratios of the four borehole sections compared with the range of inferred Critical Zone (CZ) and Main Zone (MZ) parental magmas of the Bushveld Complex, as represented by B1 and B2/B3 compositions of fine-grained marginal sills (Curl, 2001). (a) Average values and 2σ standard deviations for Nb/U and U/Th for the lower pyroxenite (L. pyrox, open symbols and dashed lines) and upper pyroxenite (U. pyrox, closed symbols and continuous lines) in the four sections studied in relation to the fields for parental magma compositions. (b) Average values and 2σ standard deviations for U/La and Th/Nb for the lower and upper pyroxenites in the four sections studied in relation to the fields for parental magma compositions. Symbols as for (b). (c) Variation in Th/Nb vs normative plagioclase content for core SD22. Symbol types define a series of arrays for contiguous samples in the vertical profile (same symbols). Compositions for mean CZ and MZ magmas are shown. hwn, hanging-wall norite; up, upper pyroxenite; tCr, top reef chromitite; lpP, lower pegmatoidal feldspathic pyroxenite; lpF, lower feldspathic pyroxenite; bCr, bottom reef chromitite; fwn, foot-wall norite and pyroxene anorthosite.

for the sections higher in the sequence to have higher Th/Nb values, or greater affinity with the Critical Zone (CZ) parent magma.

Systematic variations in the abundances of trace elements through the four reef sections studied show broadly similar patterns, but in detail are different for each core. Typical patterns are illustrated for Ta, U, and Zr (Fig. 6). The overall concentrations of these elements are highly variable and are characterized by regular oscillations on a scale of 20–50 cm, resulting in a series of peaks and troughs. This pattern is most obvious in the lower pyroxenite, within which there is also a general tendency for the concentrations to increase upwards, particularly in core sections SD45 and SD46. There is excellent correspondence for the variations of Ta, U, Th, and Nb (not shown), but there is no direct lithostratigraphic correlation in pattern form between the different borehole sections. In the upper pyroxenite there is a general trend of an initial increase followed by a decrease upwards in the sections. Zr exhibits similar patterns to Ta, Nb, U and Th, but has a lower degree of correspondence compared with these highly incompatible trace elements.

The two deflections of SD22 (D3 and D5) show similar distributions for all elements and broadly the same structure of peaks and troughs, although the fine detail is different. The patterns of peaks and troughs are displaced downwards in D5 relative to D3 by about 0·5 m relative to the datum of the top chromitite, indicating the lateral scale on which such variations occur.

Average cumulative trace element contents of the Merensky Reef

Average cumulative trace element contents provide a comparison of the bulk trace element compositions in the four sections studied (Fig. 7). Cumulative values help overcome the possible problem of small-scale decoupling of the trace elements as a result of crystallization of

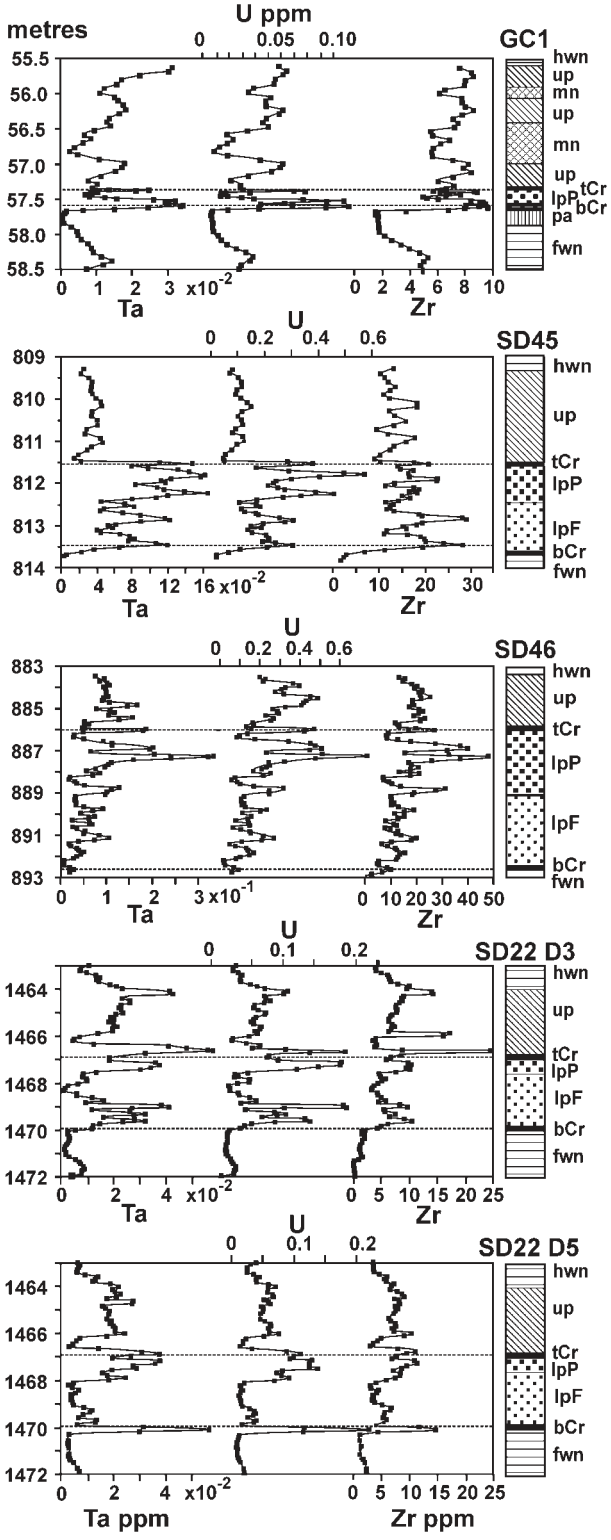

Fig. 6. Stratigraphic variation of the bulk-rock concentrations of the incompatible trace elements Ta, U and Zr in each of the sections, including the D3 and D5 deflections for SD22. Abbreviations of rock-types in columns as in Fig. 3. (Note changes in concentration scales for the different sections.)

late-stage minerals, and are representative of the entire rock units. The value for each element is determined by sequentially adding, from the base of the pyroxenite upwards, the thickness of the core sample (m) multiplied by the element concentration (as μg/g or ppm), and dividing by the total thickness of the section analysed (m). Inter-element plots of the highly incompatible trace elements Nb, Ta, Th and U are close to linear with a small deviation (Fig. 7), and the regression lines in these plots (except for Zr) intersect close to the origin. Plots of Zr (Fig. 7a) and Hf (not shown) against the highly incompatible elements are also approximately linear but do not intersect at the origin because of incorporation of Zr and Hf in early formed cumulus orthopyroxene, as these elements are not highly incompatible. This intercept allows an estimate of the amount of Zr and Hf incorporated into cumulus phases, mainly orthopyroxene. It is therefore not advisable to use uncorrected whole-rock Zr contents to define parental magma signatures (e.g. Eales, 2002).

The degree of correlation indicates consistent bulk trace element compositions between the four sections and also suggests that selective decoupling and partial removal of these elements from the cumulate pile did not occur. In Table 2 these ratios are compared with crustal and mantle values, and for the various proposed Bushveld liquids.

The relative average cumulative incompatible element abundances reflect either the effects of fractionation by which these elements became concentrated in the magma, or the relative amounts of trapped liquid in the four sections. Section GC1 has the lowest incompatible trace element contents, and is used as a comparison for the other sections (Table 3). Section SD46 has approximately five times the concentration of incompatible trace elements compared with GC1; SD22 and SD45 are intermediate between SD46 and GC1. If fractionation of the magma was responsible for the differences in incompatible element concentration then this should be reflected in the average Mg-number for the whole-rocks [calculated as molecular MgO/(MgO + FeO); Table 3]. Mg-number does not indicate marked differences that may reflect significantly different degrees of fractionation in the four sections. Indeed, it shows the opposite effect of higher incompatible element contents correlating with higher Mg-number. The determination of average Mg-number excluded samples of the underlying pyroxene anorthosite, which are in all cases less than 0·75.

The role of plagioclase

Plagioclase in the Merensky Reef is typically interstitial, or more rarely, present as strongly zoned laths. However, that does not necessarily mean that it crystallized entirely from trapped liquid in the pyroxene mush.

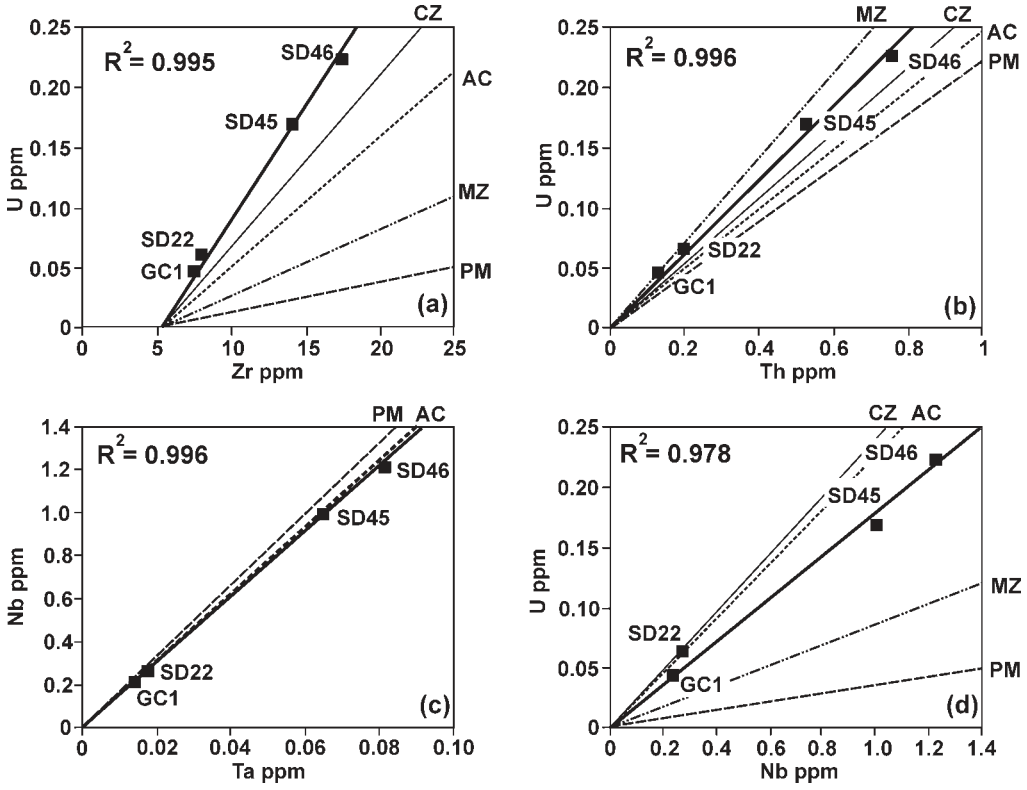

Fig. 7. Inter-element plots of average cumulative incompatible trace element contents for each of the sections. The method of calculation is described in the text. The ratios of the trace elements for CZ and MZ magmas [respectively from the B1 and B2/B3 compositions of Curl (2001)], primitive mantle (PM) (Sun & McDonough, 1989) and average upper and middle continental crust (AC) (Rudnick & Gao, 2003) are shown as lines on the diagram. The bold lines are regressions through the borehole data points. (a) Plot of U vs Zr indicates that 5–6 ppm Zr is contained within the early formed cumulus minerals in the Merensky Reef. To compare ratios in this plot, the intercepts for PM, AC, CZ and MZ have been adjusted to 5·5 ppm Zr on the abscissa. (b) U vs Th indicates the intermediate compositions between CZ and MZ liquids. (c) Nb vs Ta illustrates the strong crustal signature of the Merensky sections. CZ and MZ magma compositions are not shown because of lack of agreement between the Ta data of Curl (2001) and recent determinations of the sills (A. Wilson, unpublished data on marginal sills). (d) U vs Nb indicates that compositions are close to average upper and middle crust, and are overall closer to CZ than MZ magma types.

A plot of Eu* (the Eu anomaly calculated to be the difference between normalized measured Eu concentration and that extrapolated from the abundances of the adjacent REE) vs Sr (Fig. 8a) shows a strong positive correlation where Eu* is positive reflecting the oikocrystic growth of plagioclase, or the early development of cumulus cores. For strongly negative Eu* (< –2), Sr increases slightly with increasingly negative Eu*, and therefore is probably related to the dominant effect of the liquid composition, as opposed to oikocrystic or cumulus plagioclase. Each drill core section exhibits a different trend in Fig. 8a, with SD22 having a trend that is distinctly different from the other sections.

The degree of dispersion of highly mobile elements (such as Rb and K) relative to immobile incompatible elements could reflect the role of hydrous fluids. A plot of Rb vs (Nb + Ta + Th + U) for all sections (Fig. 8b) reveals a strong linear correlation with minor dispersion occurring only at very low Rb concentrations (0·5–2 ppm). Overall, the concentration of Rb in SD22 is consistently slightly higher than in the other sections and is probably indicative of relatively higher amounts of oikocrystic or cumulus plagioclase (also resulting in the more positive Eu* values) in this section.

CHARACTERIZATION OF RARE EARTH ELEMENT PATTERNS IN THE MERENSKY REEF

All bulk-rock samples were characterized in terms of their chondrite-normalized REE pattern shape and Eu anomalies (Eu*). Three types of patterns were defined on the basis of Eu*: Type 1—samples exhibiting strong positive Eu*; Type 2—small or no Eu anomaly; Type 3—strong negative Eu*. Within these groups further subdivisions can be made based on the shape of the REE patterns [defined by steep light rare earth element (LREE)-enriched, flat, and U-shaped patterns; subdivided as types 1/1–1/3, 2/1–2/3, etc.]. Overall,

Table 2: *Ratios of incompatible trace elements based on average cumulative totals compared with crustal and mantle abundances, and proposed Bushveld magmas*

	Nb/U	Th/Nb	Th/U	Ta/Nb	Ta/U	Ta/Th	Zr*/Th	Zr*/Hf*
Borehole								
SD45	5·88	0·53	3·10	0·064	0·38	0·122	18·93	34·97
SD46	5·39	0·62	3·35	0·066	0·36	0·107	17·37	36·46
GC1	5·97	0·57	3·43	0·062	0·37	0·108	28·24	42·77
SD22	3·83	0·76	2·93	0·078	0·30	0·102	19·66	37·53
Average	5·12 ± 0·99	0·63 ± 0·10	3·18 ± 0·23	0·069 ± 0·007	0·35 ± 0·04	0·109 ± 0·008	21·05 ± 4·88	37·93 ± 3·39
Av. middle and upper crust[1]	6·1	0·76	4·44	0·065	0·40	0·09	23·6	34·00
Upper crust[1]	4·44	0·88	3·80	0·08	0·33	0·09	18·4	36·4
Lower crust[1]	25·0	0·24	6·0	0·12	3·0	0·50	56·0	35·8
Primitive mantle[2]	33·9	0·12	4·04	0·06	1·95	0·48	131	36·25
CZ magma (B1[3])	4·05	0·87	3·53	0·12†	0·501†	0·15†	22·42	40·81
MZ magma (B2/B3[3])	11·3	0·33	3·2	0·12†	1·49†	0·49†	55·65	39·8

*Zr and Hf recalculated to correct for their incorporation into early formed silicate phases on the basis of the intercepts in Fig. 7.
†New data for marginal sill samples (A. Wilson, unpublished data) indicate that the Ta analyses of Curl (2001) may be high by as much as 30%. Therefore, comparative ratios involving Ta for Bushveld liquids may not be valid.
References: [1]Rudnick & Gao (2003); [2]Sun & McDonough (1989); [3]Curl (2001).

Table 3: *Relative degrees of enrichment (compared with GC1) in incompatible elements expressed as average cumulative totals per unit thickness for each section, and for average Mg-number*

	Th	Nb	U	Ta	Zr*	Av. relative enrichment	Av. Mg-no. and no. of samples†
GC1	1	1	1	1	1	1	0·793 ± 0·014 (54)
SD22	1·52	1·08	1·41	1·13	1·49	1·33 ± 0·21	0·799 ± 0·013 (74)
SD45	4·26	4·19	3·69	4·25	4·01	4·07 ± 0·22	0·802 ± 0·011 (65)
SD46	6·10	5·11	4·92	5·35	5·26	5·35 ± 0·45	0·812 ± 0·009 (92)

*Zr recalculated to correct for the abscissa intercept in Fig. 7 as a result of incorporation into pyroxene.
†Mg-number determined for samples with Mg-number >0·75.

12 distinct patterns were observed (Fig. 9), some of which may be regarded as transitional from one type to another.

The range of REE pattern types are related to the borehole sections in Fig. 10 and arranged in order of first appearance of a particular pattern type from the base of the section. Each section has a unique signature in terms of the distribution and proportions of pattern types. All sections commence with Type 1/1 in the underlying norite with steep REE patterns and a strong positive Eu*. This is followed in most sections, at the base of the pyroxenite, by Type 1/3, which has a steep REE pattern and small positive Eu*. In SD22 this zone has a relatively flat pattern of Type 2/2 or 2/4. Upwards from this lower section the sequence changes to negative Eu* values with flat REE patterns or to alternating layers with positive and negative Eu*. The characteristic pattern, for the thicker pyroxenite in particular, is the alternation of layers with positive and negative Eu*.

In SD46, repetitions of positive and negative Eu* occur on a scale of 20–60 cm. In a few cases the cycles start with a flat pattern and no Eu anomaly. Alternating patterns of positive and negative Eu* are also observed for SD22 but these tend to be flatter or U-shaped compared with SD46. In SD45, over the first metre of the lower pyroxenite the REE patterns are generally steep with moderate to no Eu anomaly, although some are U-shaped and close to symmetrical. The upper part of the lower pyroxenite has slightly flatter REE patterns with strong negative Eu*. The upper pyroxenite has U-shaped patterns with strong negative Eu*. In GC1 the pattern types are similar to SD22 with several repeated

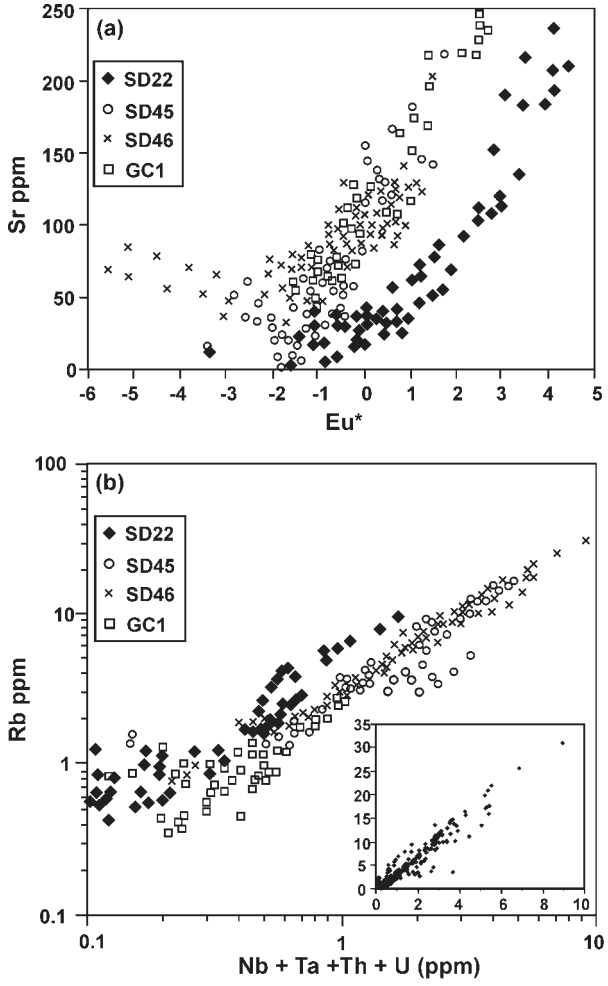

Fig. 8. Variation of trace elements associated with plagioclase. (a) Sr vs Eu*, (b) Logarithmic plot of Rb vs (Nb + Ta + Th + U). The inset is the same graph shown as a linear plot.

sequences. The general trend is one of steep REE patterns and strongly positive Eu* migrating upwards into flatter patterns (some also La depleted) with negative Eu*. Higher in the sequence, the patterns tend to be U-shaped with no, or small negative Eu anomaly. Towards the top of the lower pyroxenite in GC1, the patterns are relatively flat, with some samples exhibiting depletion in La and Ce, and strong negative Eu*.

Rare earth modelling for the Merensky Reef sections

Modelling of the REE patterns allows constraints to be placed on the cumulus processes, and on the possible interactions between different magma compositions. Most reliable estimates of the mineral–melt partition coefficients (D) for orthopyroxene pertain to medium- or high-pressure conditions and compositions appropriate for mantle melting (E. Hauri, personal communication, 2000; McDade *et al.*, 2003). These D values are a factor of two or three times lower than those suggested as being appropriate for basaltic melts at moderate pressures (Rollinson, 1993). The effect of liquid composition is well documented (Blundy & Wood, 2003; Nielsen, 2004) and there is a tendency for the ratio of D_{La}/D_{Yb} to decrease in more silica-rich magma compositions (Green & Pearson, 1985; Green, 1994), which would be appropriate for Bushveld-type magmas. The orthopyroxene–melt partition coefficients used in this study are based on estimates for mid-ocean ridge basalts (MORB; Asimow & Langmuir, 2003; McDade *et al.*, 2003), but increased by 10% to account for the higher silica content in the Bushveld magmas. The most consistent plagioclase–melt partition coefficients are those reported by McKenzie & O'Nions (1991), but these are generally somewhat higher than measured values. Therefore, the mean has been taken of those obtained from theoretical considerations (McKenzie & O'Nions, 1991) and those reported in the MORB project database (http://www.petdb.org). The partition coefficients used in this study are given in Table 4.

The observed REE patterns were modelled using combinations of the CZ and MZ magma compositions. Modelling involved fractionation, representing early stage open-system growth of the liquidus mineral assemblage, and the final combination of orthopyroxene, liquidus plagioclase and trapped liquid. Similar constraints on liquid compositions have been modelled for the cumulates of the Bjerkreim–Sokndal intrusion, Southern Norway (Charlier *et al.*, 2005).

The steep, Eu-enriched REE patterns observed in the footwall pyroxene anorthosite or norite can be modelled using appropriate proportions of pyroxene (3–10%) and plagioclase (90–97%) and small amounts (<2%) of trapped liquid. The REE patterns of the pyroxenite are modelled using a fractionated mixture of the CZ and MZ magmas in equilibrium with plagioclase and orthopyroxene. In some cases better agreement is obtained by initially using one of the parent liquid derivatives, and then mixing with the second liquid. Some degree of fractionation (5–30%) is required to significantly change the slopes of the patterns, indicating that the system must have been open during the initial stages of cumulate formation. Where the proportion of the trapped liquid exceeds 3–5%, it has the major influence on the REE pattern and bulk-rock REE concentrations. Where the trapped liquid component is low (<3%), the REE patterns are mainly controlled by the abundances of cumulus mineral phases.

Fractionation of plagioclase within the cumulate pile is required to produce the strongly negative Eu anomalies in the residual liquids, whereas accumulation of plagioclase as oikocrysts results in positive anomalies. This

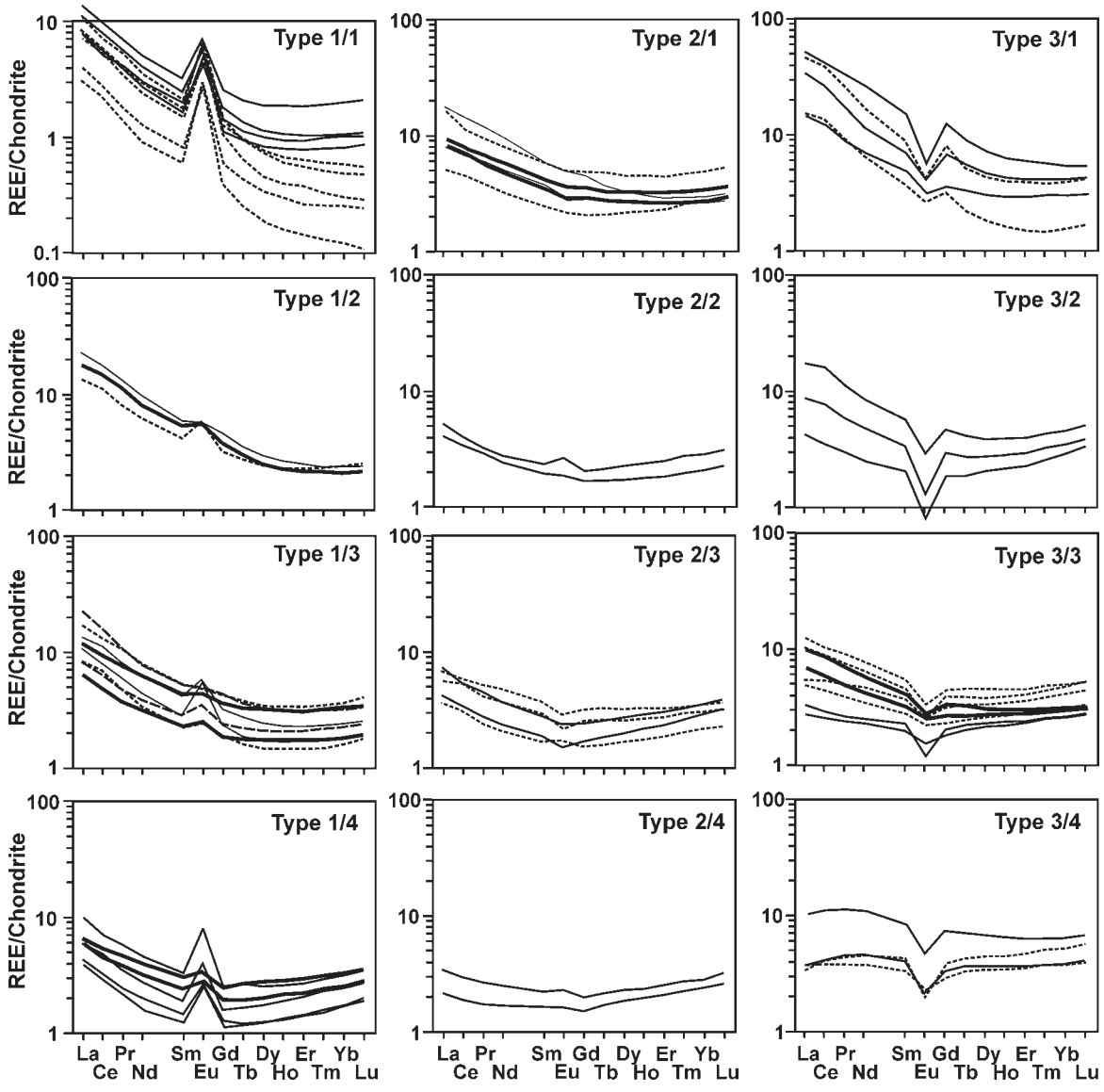

Fig. 9. Chondrite-normalized REE patterns for all rock-types in the sections studied classified into three main groups defined principally on the size and type of Eu anomaly, and then into four subgroups based on the shape of the overall profile. Type 1 pattern is defined on the basis of a positive Eu anomaly; Type 2 has no, or only minor Eu anomaly; Type 3 has a negative Eu anomaly. Further sub-types are based on the shape of the overall pattern, which has four subsets within each group. Variants within those groups are shown by different line styles. Chondrite normalization data from Sun & McDonough (1989).

indicates migration of liquid on at least the scale of the REE pattern-types shown in Fig. 10. Flat or U-shaped patterns are consistent with low trapped liquid contents and are controlled mainly by orthopyroxene, which tends to produce heavy rare earth element (HREE) enrichment. Accumulation of plagioclase as oikocrysts or cumulus crystals results in LREE enrichment. The combination of these controls results in U-shaped patterns.

The final mixture before complete solidification of the rock comprises cumulus orthopyroxene, plagioclase oikocrysts (or in some cases cumulus plagioclase) and differentiated trapped melt. The results of the modelling representing the various pattern types are illustrated in Fig. 11 and Table 4. The least satisfactory models are those for the footwall pyroxene anorthosite. In these rocks the modelled patterns (Type 1/1) are generally steeper, and the positive Eu* is larger than actually observed. The modelling does not provide unique solutions because of the number of variables involved. However, the following observations are robust. (1) Most patterns require a combination of Critical Zone and

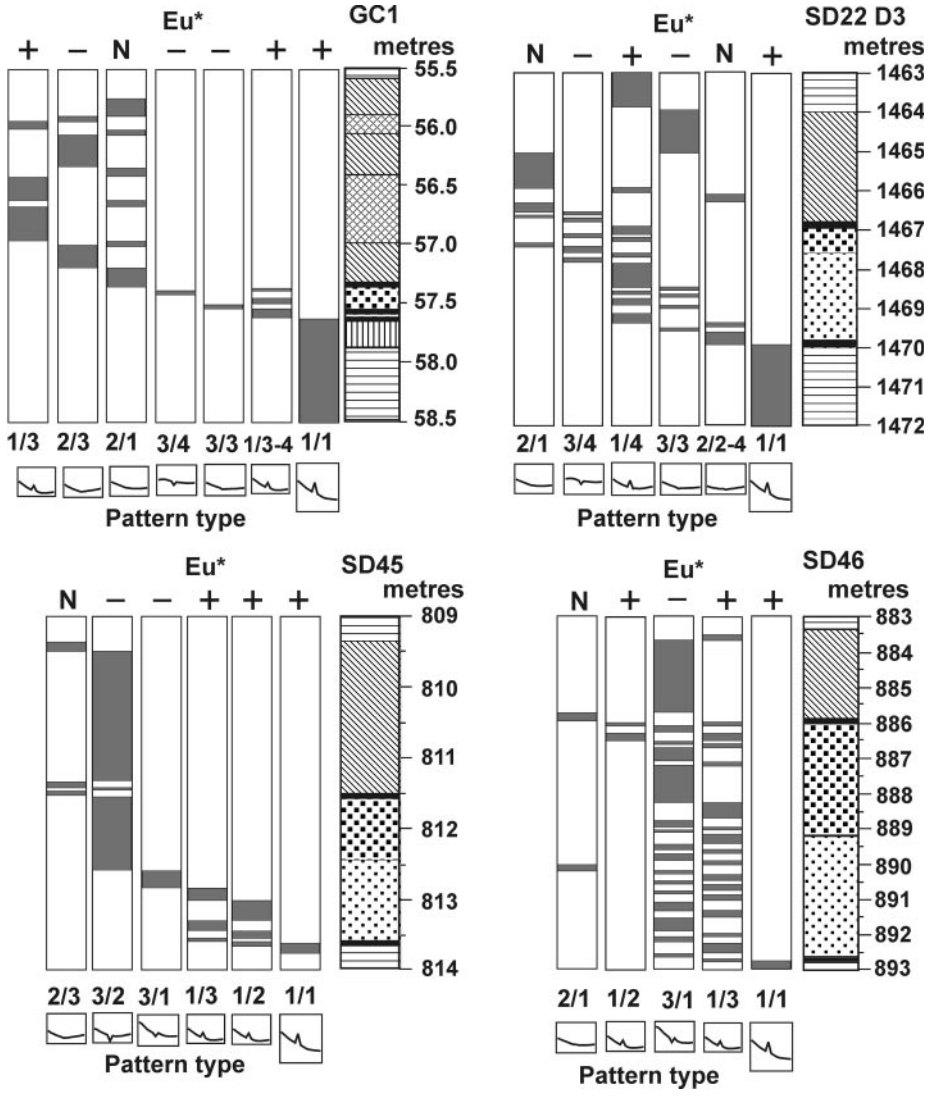

Fig. 10. Distributions of REE pattern types through each of the drill core sections. Types with positive (+), negative (–), and no (N) Eu anomaly (expressed as Eu*) are grouped in columns and the specific pattern type is classified according to the designation in Fig. 9. Thumbnail diagrams also summarize the pattern types. The grey shaded areas represent the frequency and occurrence of specific pattern types.

Main Zone-type magmas in differing ratios ranging from dominantly CZ (for some even 100%), to 30% CZ and 70% MZ. For most samples no one magma type can produce the observed range of compositions. (2) Plagioclase crystallized as an early stage phase in some sections with extensive postcumulus overgrowth, or formed entirely from the interstitial liquid. (3) Some degree of fractionation (usually 5–30%) of the interstitial liquid is required to produce the observed steeper REE patterns.

REE patterns and magma compositions

A well-defined relationship exists between abundances of the highly incompatible elements (Nb, Ta, Th, U) and the total REE (Fig. 12a). However, the non-constant ratios between these two groups of elements result from the relatively high degrees of incorporation of REE in early formed silicate minerals, compared with the incompatible trace elements. Increasing amounts of trapped liquid dominate over the cumulus minerals in controlling the distribution and concentrations of REE. The Eu anomaly becomes more negative with increasing Nb + Ta + Th + U content (Fig. 12b). This indicates that the trapped liquid dominating the REE patterns had a small to moderate negative Eu anomaly resulting from plagioclase fractionation.

The slopes of the REE patterns (expressed as $[La/Yb]_N$) are shown in relation to the total incompatible element (Nb + Ta + Th + U) content in Fig. 13. In the

Table 4: Comparison of observed and modelled rare earth element patterns

Norm	Opx K_d	Plag K_d	SD46 3/1[1]			SD45 1/1[1]			SD22 D3 1/4[1]		
			Liquid[2]	Obs	Calc	Liquid[2]	Obs	Calc	Liquid[2]	Obs	Calc
La	0·006	0·216	120·9	43·9	44·1	51·2	5·6	10·7	39·7	5·9	5·6
Ce	0·010	0·160	104·5	40·8	38·1	39·8	3·9	6·2	30·6	4·4	4·2
Pr	0·014	0·136	86·5	32·6	31·6	32·0	2·7	4·2	24·9	3·6	3·4
Nd	0·019	0·112	70·9	24·5	26·0	25·6	1·9	2·8	20·2	3·0	2·8
Sm	0·043	0·088	40·1	14·0	15·3	16·0	1·1	1·4	13·8	2·3	2·1
Eu	0·064	0·584	16·3	5·3	6·8	15·1	4·4	5·9	14·9	3·5	3·4
Gd	0·099	0·053	23·1	11·4	9·5	11·2	0·75	0·61	9·9	2·0	1·9
Tb	0·130	0·048	16·8	8·0	7·2	9·3	0·49	0·47	8·5	2·0	1·8
Dy	0·155	0·044	13·4	6·3	6·0	7·9	0·38	0·37	7·5	2·1	1·8
Ho	0·185	0·038	11·5	5·6	5·3	7·4	0·29	0·32	7·1	2·1	1·8
Er	0·220	0·033	10·1	5·3	4·9	6·8	0·28	0·26	6·7	2·2	1·9
Tm	0·290	0·029	8·9	4·9	4·7	6·7	0·25	0·24	6·6	2·5	2·2
Yb	0·330	0·025	8·7	4·7	4·8	6·8	0·23	0·23	6·6	2·6	2·4
Lu	0·383	0·020	8·6	4·8	5·0	7·0	0·21	0·22	6·9	2·8	2.·8
La/Sm				1·8	2·9		3·0	3·8		2·0	2·0
Gd/Lu				2·4	1·9		3·5	2·8		0·7	0·7
La/Lu				9·2	8·8		26·4	49·3		2·1	2·0
Eu*				–7·4	-5·6		3·5	4·9		1·4	1·4
Initial modelled liquid mixture CZ:MZ magmas				70:30			40:60			20:80	
Fractionating phases from initial liquid Opx:Plag				60:40			5:95			60:40	
Added evolved liquid after 30% fractionation				5%			5%			5%	
Final mixture Opx:Plag:trapped liquid in wt %				65:5:30			3:97:0			77:12:11	

Norm	Opx K_d	Plag K_d	SD22 D3 2/4[1]			GC1 3/3[1]			SD45 1/3[1]		
			Liquid[2]	Obs	Calc	Liquid[2]	Obs	Calc	Liquid[2]	Obs	Calc
La	0·006	0·216	44·9	2·6	2·7	55·2	3·8	4·4	42·3	17·9	13·9
Ce	0·010	0·160	34·3	2·3	2·3	45·7	4·1	4·1	32·5	14·0	10·1
Pr	0·014	0·136	27·4	2·1	2·0	38·4	4·0	3·8	26·1	6·0	6·2
Nd	0·019	0·112	21,7	2·0	1·8	32·4	4·2	3·7	20·9	6·0	6·2
Sm	0·043	0·088	13·9	1·8	1·6	21·9	3·8	3·7	13·8	4·0	4·1
Eu	0·064	0·584	13·9	1·8	1·7	15·3	2·2	2·3	14·4	6·4	6·6
Gd	0·099	0·053	9·8	1·7	1·9	15·5	3·5	4·3	9·8	3·3	3·1
Tb	0·130	0·048	8·2	1·9	1·9	12·6	3·9	4·0	8·3	2·7	2·7
Dy	0·155	0·044	7·1	2·1	1·8	10·7	4·0	3·7	7·3	2·5	2·4
Ho	0·185	0·038	6·7	2·2	1·9	9·8	4·2	3·7	6·9	2·4	2·4
Er	0·220	0·033	6·2	2·3	2·0	8·9	4·3	3·7	6·5	2·4	2·3
Tm	0·290	0·029	6·2	2·6	2·4	8·3	4·5	3·9	6·4	2·4	2·5
Yb	0·330	0·025	6·2	2·7	2·7	8·2	4·7	4·1	6·4	2·6	2·7
Lu	0·383	0·020	6·5	3·0	3·1	8·3	5·0	4·6	6·7	2·8	2·9
La/Sm				1·4	1·7		0·9	1·2		4·4	3·3
Gd/Lu				0·6	0·6		0·7	0·9		1·2	1·0
La/Lu				0·9	0·9		0·8	0·9		6·9	5·2
Eu*				0·0	0·0		–1·4	-1·7		2·7	2·9
Initial modelled liquid mixture CZ:MZ magmas				40:60			30:70			50:50	
Fractionating phases from initial liquid Opx:Plag				40:60			40:60			40:60	
Added evolved liquid after 30% fractionation				3%			4%			5%	
Final mixture Opx:Plag:trapped liquid in wt %				92:5:3			88:10:2			55:25:20	

[1]Rare earth pattern type from Fig. 9.
[2]Liquid composition modelled from a combination of B1 and B2/B3.

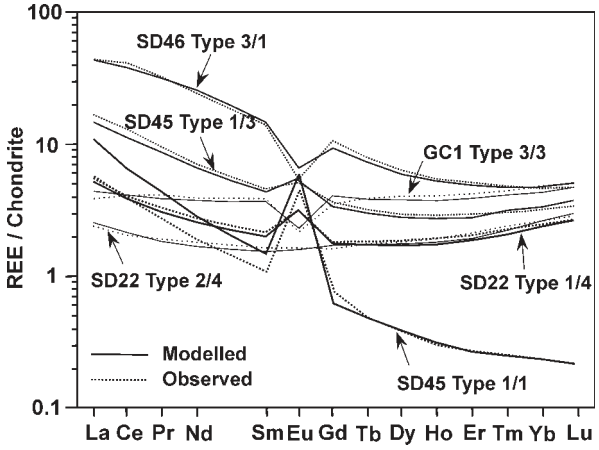

Fig. 11. Observed and modelled REE patterns (Table 4) for a selection of pattern types from each of the sections.

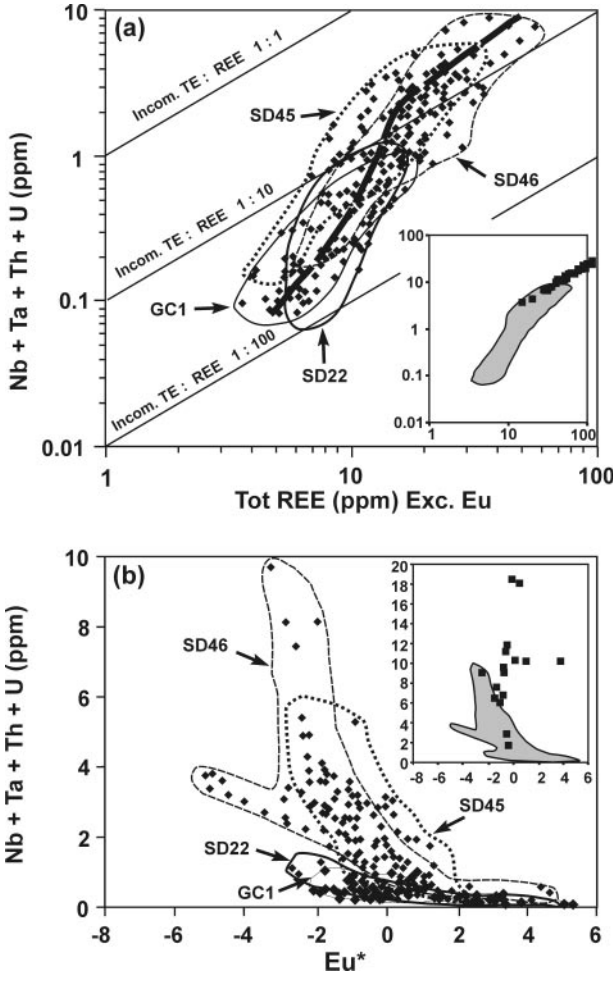

Fig. 12. (a) Total REE (excluding Eu because of its control by plagioclase) vs total incompatible element (Nb + Ta + Th + U) content. The non-linear dependence at low concentrations is because of incorporation of REE into early formed cumulus and oikocryst phases even where trapped liquid contents are low. At higher amounts of trapped liquid the ratio of REE to incompatible element contents becomes approximately constant (bold dashed line). The diagonal lines are constant ratios of the incompatible trace elements (TE) to total REE. The inset shows the distribution and overlap of the data field (grey shaded area) in relation to the marginal sill compositions (square symbols). (b) Total incompatible element concentrations plotted against Eu* indicate the increasingly negative Eu* with increasing trapped liquid content. In the inset figure the dataset is shown in relation to the compositions of the marginal sills (square symbols).

pyroxenites the REE patterns become steeper ($[La/Yb]_N > 1$) as the total incompatible element content increases. Flat REE patterns ($[La/Yb]_N \sim 1$) are the result of the dominating influence of cumulus orthopyroxene crystallizing from a relatively evolved liquid. The footwall norite has higher $[La/Yb]_N$ as a result of increased cumulus plagioclase content. Some groups of pyroxenite (mainly from SD46) exhibit opposite behaviour in which $[La/Yb]_N$ decreases (i.e. the REE patterns become flatter) with increasing incompatible element content. The compositions of the Bushveld marginal sills overlap with the high $[La/Yb]_N$ end of the Merensky Reef dataset (inset to Fig. 13). Although some of these compositions are undoubtedly crystal enriched, there is a strong compositional similarity with the Merensky Reef data.

Variation of Eu* and sulphide content

Sulphide, and for the most part, plagioclase, are interstitial to the network of cumulus pyroxenes in the pyroxenite layers. As noted in the previous section, plagioclase may variably have crystallized either from late-stage trapped liquid, or as early formed oikocrysts, or more rarely as cumulus crystals. Eu* ranges overall from +6 to –5 reflecting the contrasting influence of early formed plagioclase oikocrysts (giving positive Eu*) or the trapped liquid (with negative Eu* signature).

The variation of S and Eu* with stratigraphic height for all sections indicates broad-scale contrasting patterns (Fig. 14a and c). Although a simple linear relationship is not observed between S and Eu* for the complete dataset, individual arrays for sets of contiguous samples indicate a strong dependence between Eu* and sulphide content (shown for SD46 and GC1 in Fig. 14b and d) for specific stratigraphic sections. From these relationships plagioclase is indicated to have influenced the distribution of immiscible sulphide liquid.

DISTRIBUTION OF PLATINUM GROUP ELEMENTS AND GOLD

In mafic layered intrusions, the PGE and Au are trace elements that are generally regarded as having being derived from outside the immediate layers that host them. Sulphide is likely to have formed as a dense,

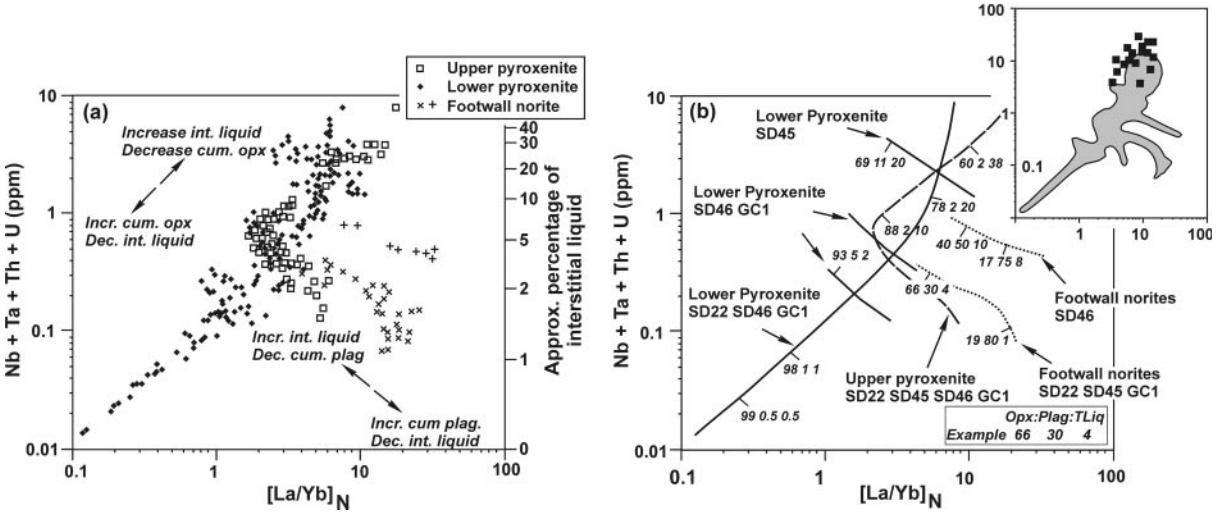

Fig. 13. Relation between total incompatible element (Nb + Ta + Th + U) content and $[La/Yb]_N$. (a) Combined data for all sections distinguished for footwall norite, and upper and lower pyroxenite. Controls are shown for relative influences of cumulus orthopyroxene and interstitial liquid, and cumulus plagioclase and interstitial liquid. The dominant trend illustrates the steepening of the REE pattern as a result of increasing amounts of trapped liquid (approximate scale for the amount of interstitial liquid is shown) reflected by the total incompatible trace element content. Crystallization of orthopyroxene leads to lower $[La/Yb]_N$, whereas plagioclase results in an increase. (b) The same trends as in (a) with proportions of modelled liquidus phases (Opx, orthopyroxene; Plag, plagioclase) and trapped liquid (TLiq) indicated. The inset figure shows the distribution of data (grey shaded field) in relation to marginal sill compositions (square symbols) (Curl, 2001).

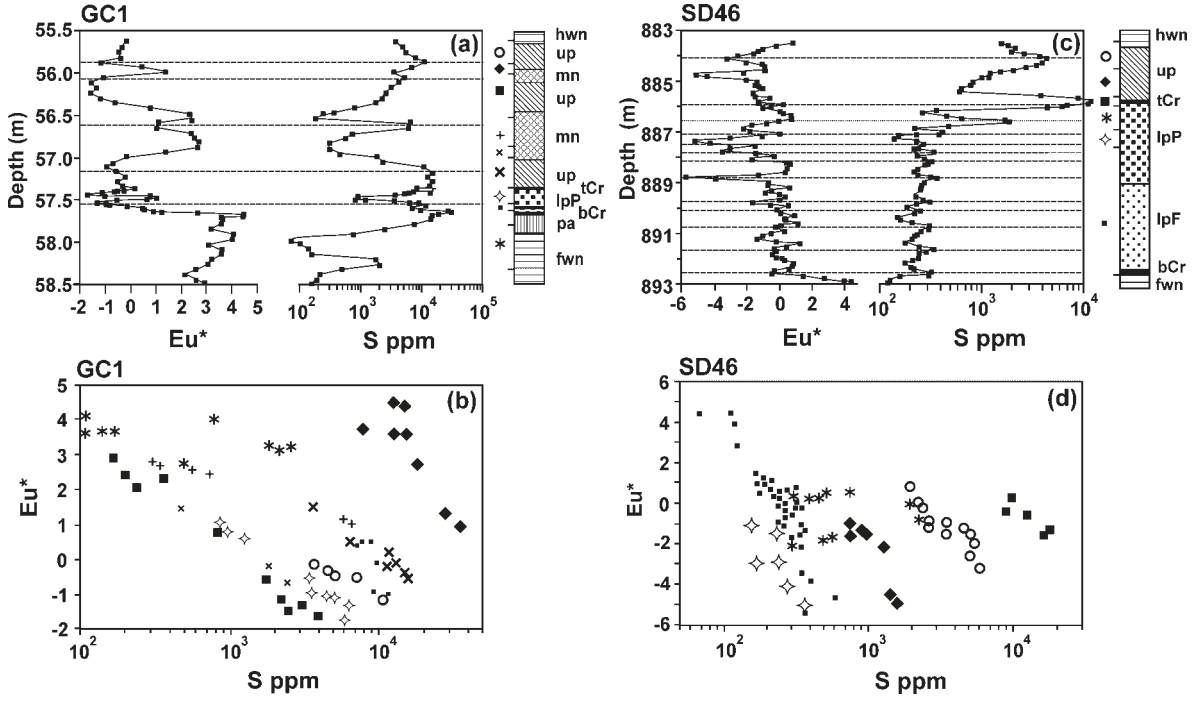

Fig. 14. Variation of Eu* and S in GC1 and SD46. (a) Variation of Eu* and S as a function of depth in section GC1. (b) Relative dependence of Eu* on S over intervals of contiguous samples indicated by the symbols and on the stratigraphic column. (c) As for (a) in section SD46. (d) As for (b) in section SD46. Symbol abbreviations in columns as for Fig. 3. Dashed lines correspond to S peaks.

immiscible liquid that accumulated with the silicate cumulates (Naldrett *et al.*, 1987, 1990). Fluids may also have been responsible for transport or remobilization of PGE (Boudreau & McCullum, 1992; Boudreau & Meurer, 1999). At present, for the Merensky Reef, there is little information on the specific links between the PGE distributions and other trace elements arising from the silicate framework of the mineralized zone.

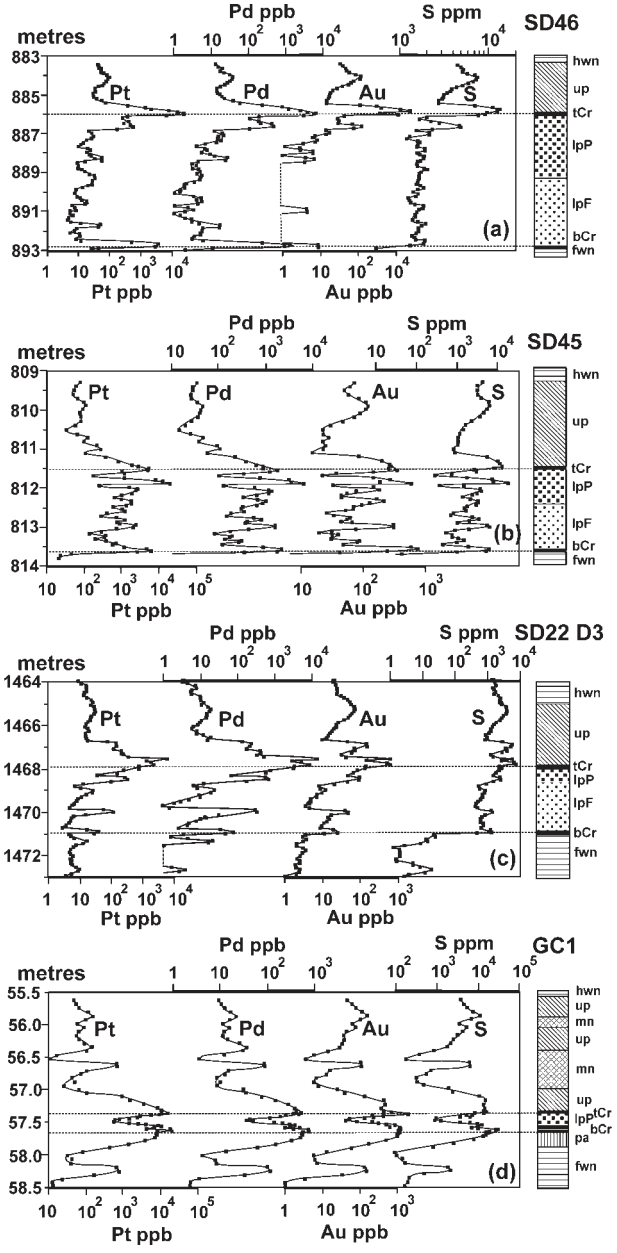

Fig. 15. Stratigraphic variations of Pt, Pd, Au and S for the four drill core sections. Symbol abbreviations in columns as for Fig. 3. (Note scale changes between sections.) Depth (metres) relative to borehole collars.

Concentration profiles and element ratios

Concentration profiles are shown for Pt, Pd, Au and S in the four sections studied (Fig. 15). In each section the distributions of these elements are similar, indicating the dominant control by sulphide, but not necessarily the only control. Concentrations of these elements increase overall upwards in the sections through a series of peaks and troughs and then decrease markedly at the base of the upper pyroxenite. The drop-off is, in all cases, significantly greater for Pt and Pd than it is for Au. S also decreases sharply at this point but then rises again in the upper pyroxenite layer, which is largely devoid of PGE. In all sections (including the thin reef section GC1), smooth distributions are observed in the upper pyroxenite layer and there is almost perfect correspondence between Au and S, underlying the strong control by sulphide on the Au content. The sulphide and PGE trends in the upper pyroxenite are similar to other PGE-enriched disseminated sulphide zones (such as the MSZ of the Great Dyke, Zimbabwe; Naldrett *et al.*, 1987; Prendergast & Keays, 1989; Wilson & Tredoux, 1990), in which removal of the PGE from the magma is considered to have occurred by precipitation of sulphide at the base of the upper pyroxenite layer.

In the lower pyroxenite all sections studied have a basal concentration of sulphide and relatively high PGE/S (tenor) dropping off rapidly immediately above the basal zone. Above this point in every section (but least developed in SD46), there is an increase in sulphide and PGE content before they again decrease. In the upper part of the lower pyroxenite there is an overall, but highly irregular, increase in sulphide and PGE content upwards in the succession.

Small-scale variations in the distributions of PGE, Au and sulphide define a series of peaks and troughs on a scale of 20–50 cm (Fig. 15). These are most clearly developed in the thicker pyroxenite of SD22 and SD46. In SD45 the variation is on a smaller scale, giving a sawtooth pattern, but again systematic variations are observed between contiguous samples. There is only a limited amount of sulphide associated with the bottom chromitite. In the narrow reef type (GC1) sulphide mineralization is developed throughout the entire pyroxenite, with a deep trough in the middle of the pyroxenite. The sulphide mineralization extends below the pyroxenite and bottom chromitite into the underlying pyroxene anorthosite.

Changes in the ratios Pt/Pd and PGE/S in conjunction with trace element distribution patterns can provide information on magma compositions, as well as primary processes such as fractional segregation of sulphides from the magma (Naldrett & Wilson, 1990). Most previous studies of the Merensky Reef have been carried out on the relatively narrow reef types (Wilson *et al.*, 1999; Barnes & Maier, 2002) and did not identify significant changes in Pt/Pd. In the three thicker reef types in this study, however, systematic changes in PGE/S and Pt/Pd are observed (Fig. 16).

High PGE tenors (PGE/S) occur at the base and the top of the lower pyroxenite (shown for SD46 and SD22 in Fig. 16a and c). In general, there is a gradual increase in PGE tenor upwards within the lower pyroxenite, commonly with several sharp spikes. The changes in

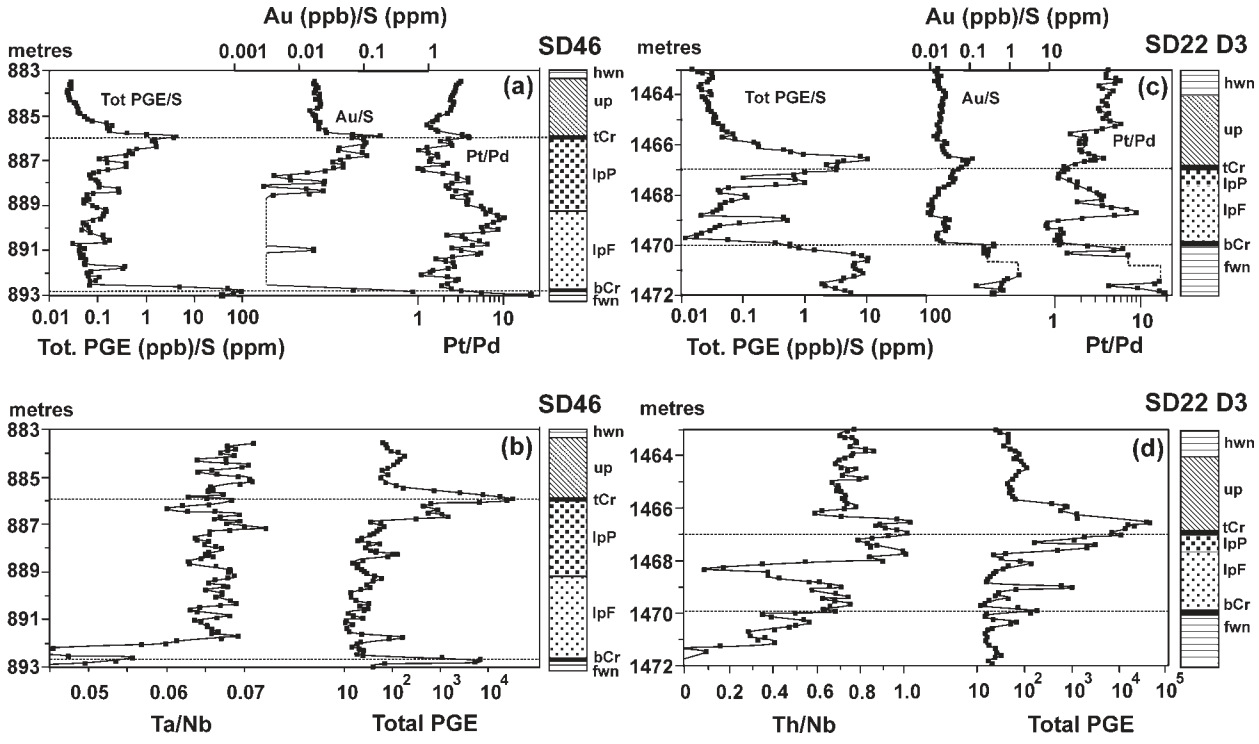

Fig. 16. Variations of total PGE, PGE to S ratios, Pt/Pd, and ratios of incompatible trace elements in SD46 (a and b), and SD22 D3 (c and d). There is not a monotonic relationship between the ratios of incompatible elements and PGE contents, but there is correspondence in sharp changes in these values. Symbol abbreviations in columns as for Fig. 3. (Note scale changes between sections.) Depth (metres) relative to borehole collars.

PGE tenor do not support the entire Bushveld magma having reached sulphide saturation prior to emplacement (see Maier & Barnes, 2005). The distribution of Pt/Pd has several distinct peaks; three are present in SD46: at the base and top of the lower pyroxenite and approximately in the centre. There is a tendency for Pt/Pd to decrease close to the base of the upper pyroxenite, but then rise again upwards in the pyroxenite.

Shown in Fig. 16b and d are patterns for total PGE and ratios of incompatible trace elements. Although there is no simple correspondence between these patterns, it is noticeable that sharp changes take place at the same, or similar, positions in each of the sections. The common feature of all the PGE patterns and Pt/Pd, and in keeping with other trace element patterns, is the regular small-scale cyclic variations.

Although there is no simple monotonic correspondence between ratios of incompatible elements and PGE content, changes in the trace element ratios correspond to changes in the small-scale variation of the total PGE content. These variations, on a scale of 0·2–1 m, are well developed in all sections, superimposed on overall systematic trends. Identical patterns for these parameters are not observed in each of the sections studied, indicating that they may be the result of interplay between different controlling processes that vary over short lateral distances (such as that between the D3 and D5 deflections of SD22). This indicates that the processes were not driven by normal magmatic differentiation in the vertical sense, but rather by strong lateral variations, which may be expected when there are interactions between different magmas that have not completely mixed. Secondary influences (such as the local migration of sulphide liquid) may have existed on scale lengths corresponding to a single sample interval.

These trace element and PGE variations are indicative of changes in magma composition controlling the distribution of trace element signatures and PGE mineralization. Precipitation of sulphide appears to only partly control the PGE distribution, and other influences would include the mixing and mingling of different magmas, the nature of the primary PGE carrier, as well as possible post-precipitation redistribution resulting from the percolation of immiscible sulphide liquid.

Cumulative contents of PGE, Cu, S and incompatible trace elements

Sulphide-associated base metals (e.g. Cu) and PGE may have been derived from a different crystallization zone from that which gave rise to the silicate cumulates. Because of its greater density, and tendency to remain in

liquid form to lower temperatures, an immiscible sulphide liquid may have percolated downwards in the crystal mush. In the same way, interstitial silicate liquid has the potential to be locally displaced. The total sulphide (or S) or PGE contents in different sections are, therefore, of importance in the petrogenetic understanding of the mineralization and its relationship with the enclosing silicates. Cumulative contents are the integrated totals for the concentrations of the metals or S over sample core lengths for continuous sections, calculated in the same way as for the trace elements, as described previously. The cumulative profiles provide information on the build-up of metal and sulphide contents through the mineralized zone and indicate relative positions of enrichment within the reef. There is a general tendency for thin Merensky Reef types to have higher concentrations (ore grade) of PGE than thicker reefs, but currently there is no information as to whether the total PGE contents are similar or different.

Cumulative curves (Fig. 17a) illustrate a generally low level of mineralization in the lower pyroxenite, with most mineralization occurring close to the boundary of the lower and upper pyroxenite layers. The thinner reef types (GC1 and SD45) have a more gradual rise in metal content than the thicker reefs (SD22 and SD46). SD45 and GC1 have relatively high PGE contents in the lower part of the pyroxenite. The contribution to the PGE metal budget from the upper pyroxenite is minimal and the cumulative curves are essentially flat from this point. There is an appreciable range in total metal contents for each of the sections.

The total mass of PGE contained within the pyroxenite for these sections appears to be related to total thickness of the pyroxenite unit (Fig. 17b). Cumulative PGE, Cu (Fig. 17c) and S (Fig. 17d) also have a strong relationship with total PGE, indicating the close association of these elements within each section. This indicates, that, at least for the sections studied here, there has been little decoupling between the base metals, PGE, and sulphide. The strong relationship between S and Cu (Fig. 17e) confirms that loss of S is probably minimal. The relationship between the total PGE content and the thickness of the enclosing pyroxenite suggests that the same processes controlled the formation of the pyroxenite and the PGE mineralization. Total PGE contents are related to trace element ratios (shown for Th/Nb in Fig. 17f) and, therefore, provide a basis for linking the mineralization process to the enclosing pyroxenite. Thicker pyroxenite and higher PGE contents correlate with trace element signatures, which indicate direct controls from the different magma types. A similar relationship has been observed for the UG-2 platiniferous chromitite (R. Hornsey, personal communication, 2006)

Data from Barnes & Maier (2002), using samples from the Impala Platinum Mine in the western Bushveld Complex, suggest similar values for Th/Nb (it should be noted that Nb is not reported in the Barnes & Maier dataset and has been estimated from Ta values using an equation relating these elements derived from this study), but the profile is different. For this narrow reef type the lower part of the pyroxenite layer, which coincides with the mineralized zone, has an average Th/Nb of 0·385. The upper pyroxenite has an average ratio of about 1·0. Such an abrupt change is not observed in the data from the drill cores used in this study, indicating that different areas of the Bushveld Complex have distinct signatures.

Primitive mantle-normalized PGE patterns and PGE ratios

Primitive mantle-normalized PGE patterns (Barnes & Maier, 1999) are shown for SD45 in Fig. 18. These values have been recalculated to 100% sulphide and are shown in order of increasing chalcophile character. The types of patterns are generally similar to those reported by Barnes & Maier (2002) for Impala and all form the characteristic arch-shaped pattern reported by Naldrett (2004) for magmatic deposits of this type. Seven pattern types can be distinguished, some of which are variants of similar broad types and represent the transition from one type to another. The pattern types are characterized by which of the elements Pt, Pd, Au and Rh occur as peak values, with further variants in which Ni, Os and Ir are approximately equal on the diagrams. The different PGE patterns are not simply related to lithology as observed for Impala (Barnes & Maier, 2002). Pattern types 1, 2 and 3, characterized by peak values for Pt, dominate the lower pyroxenite, whereas pattern type 7 dominates the upper pyroxenite. Alternations are observed with the other minor patterns, indicating that controls relating to specific small-scale layers were also operating. This is attributed to the same controls caused by the interplay of different magmas that gave rise to the trace element signatures.

Ratios of PGE on the basis of groups of elements of relative chalcophile to siderophile character [i.e. (Pt + Pd + Rh)/(Os + Ir + Ru)] have been shown to characterize the Main Zone and Critical Zone, with values of >80 and 1–20, respectively (Maier & Barnes, 1999; Kruger, 2005). PGE scavenged by immiscible sulphide droplets from combinations of CZ and MZ magmas may, therefore, also be expected to reflect these variations. Stratigraphic variations of this value are shown for boreholes SD45 and GC1 (those with higher than detection limits through most of the section) in Fig. 19. The range of values in most cases is 4–17. At the base of SD45 very high values (20–90) are shown for one group of samples, which immediately overlie the lower

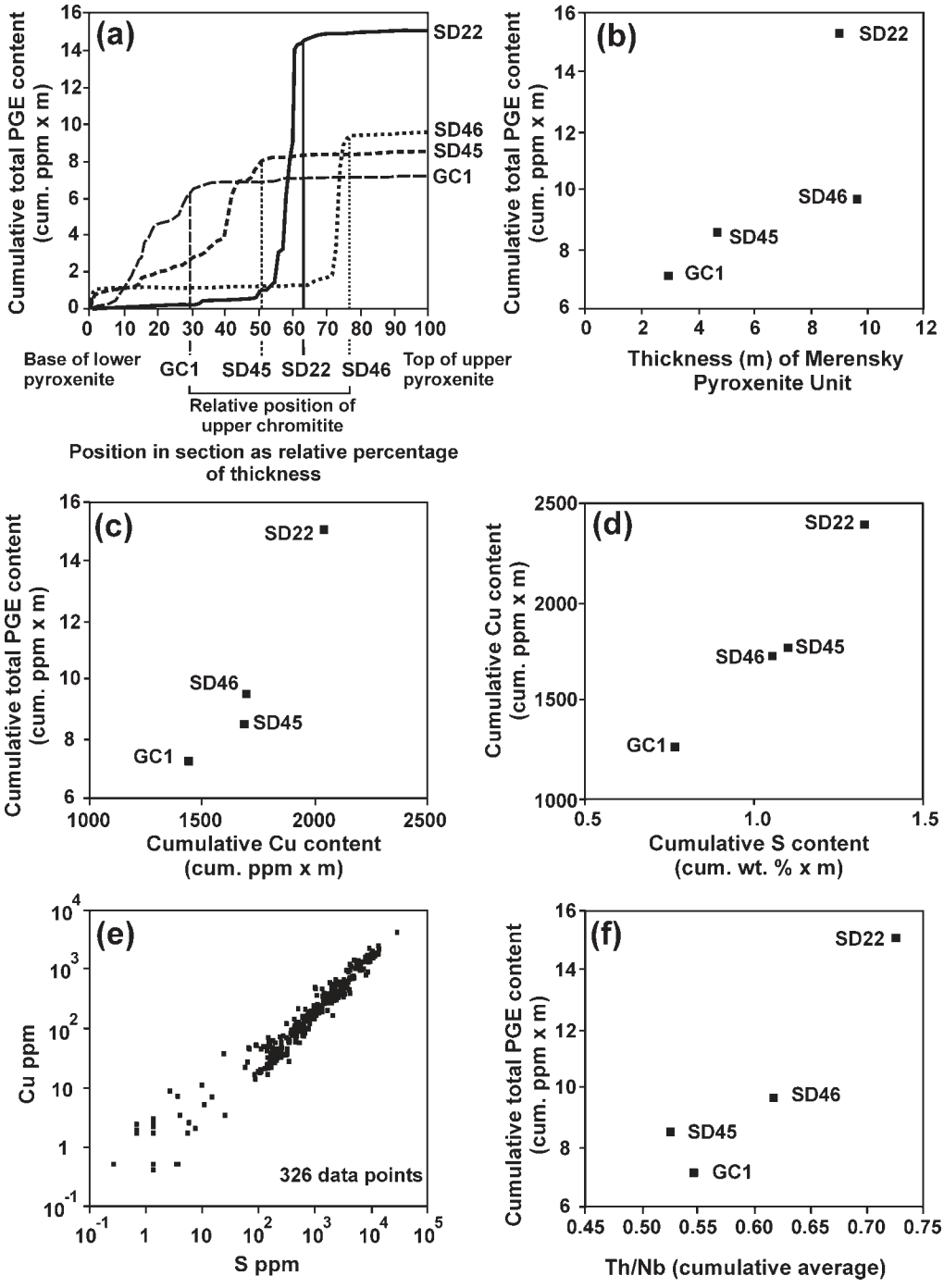

Fig. 17. Cumulative parameters for all sections relating to total PGE contents, base metals and trace elements. (a) Cumulative total PGE (excluding Au) for all sections determined from the base upwards. (b) Relationship of thickness of pyroxenite and cumulative total PGE contents. (c) Cumulative total PGE contents in relation to cumulative total Cu contents. (d) Cumulative Cu contents in relation to cumulative S contents. (e) Cu vs S contents for all sections. (f) Cumulative total PGE in relation to Th/Nb calculated as the cumulative average (cumulative value for each element per unit length of core).

chromitites. Variations in the lower pyroxenite indicate a series of changes on the same scales and for the same intervals as for other trace elements and ratios. In SD45 (Fig. 19a), the values increase gradually over two cycles corresponding to the lower feldspathic pyroxenite and the lower pegmatoidal pyroxenite. In both boreholes there is gradual, and less variable, decrease in the upper pyroxenite.

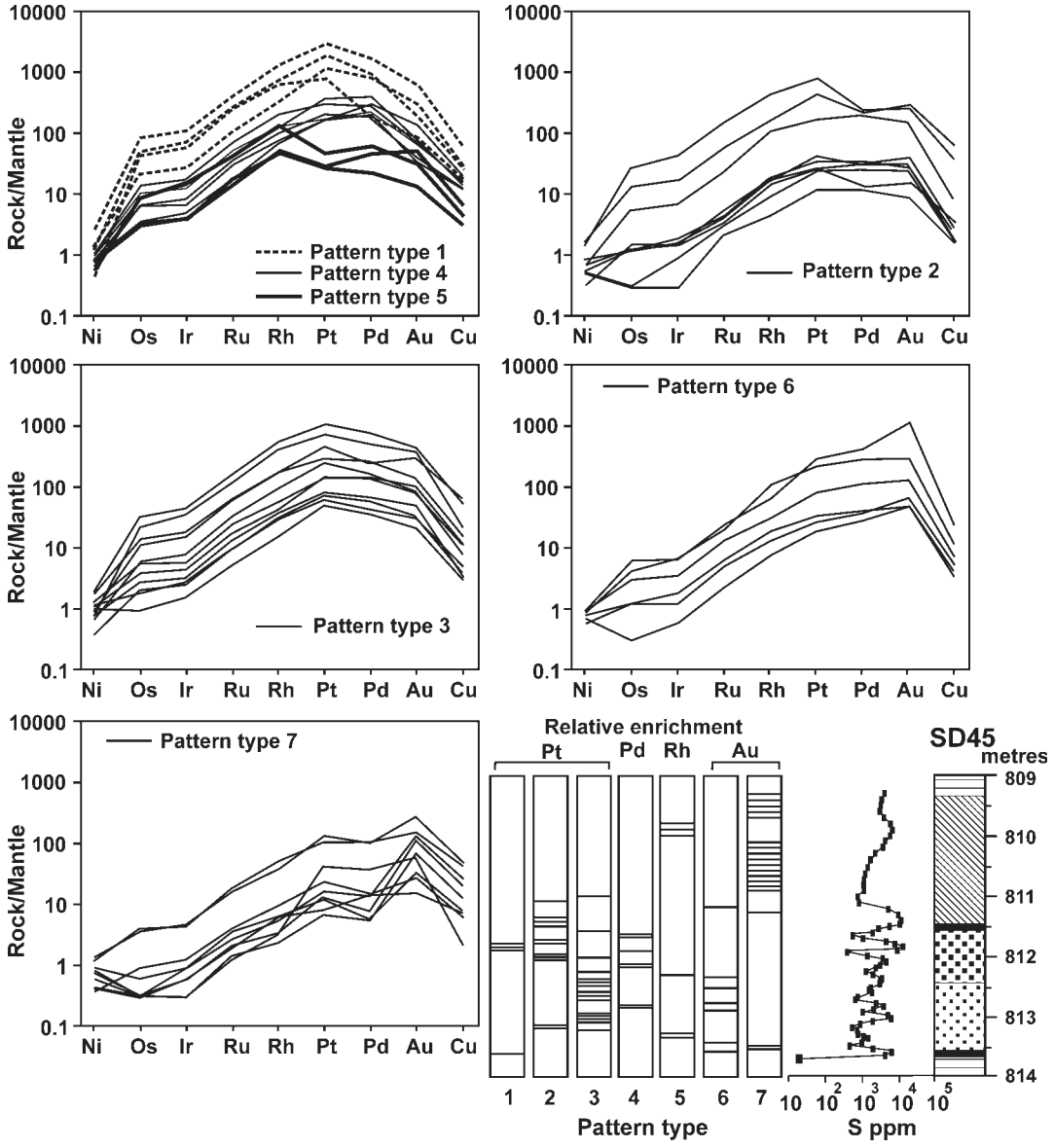

Fig. 18. Primitive mantle-normalized PGE patterns [normalization values from Barnes & Maier (1999)] recalculated to 100% sulphide for section SD45. Seven distinct PGE pattern types are observed relating to shapes of patterns, peak element and the relative concentrations of Ir to Ni. The stratigraphic column is shown together with variations in S content. Ornamentation on the stratigraphic column is the same as in Fig. 3. Within the lower pyroxenite, samples that are characterized by pattern types 1, 2 and 3 (Pt peaks) in most cases have higher S contents.

DISCUSSION

The aim of this study is to compare four sections of the Merensky Reef located in the same area of the western Bushveld Complex and to determine the extent to which whole-rock compositions and the distribution of the mineralized zones provide constraints on magmatic processes. The characteristics of these sections relate to small-scale and bulk concentrations and distributions of trace elements and PGE. The only previous comparable study is from a single occurrence of narrow-reef from Impala Platinum Mine (Barnes & Maier, 1999), which is also located in the western Bushveld Complex, south of the study area.

Incompatible element signatures

The highly incompatible (Ta, Nb, U, Th) and incompatible (Zr, Hf and REE) trace elements monitor the behaviour of the trapped liquid within the cumulus pile

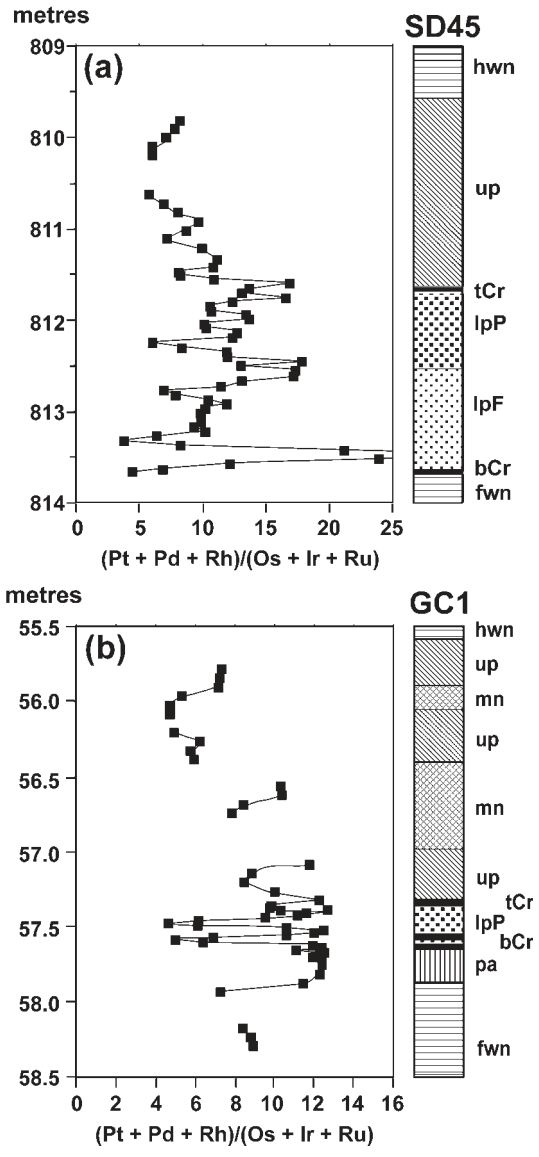

Fig. 19. Stratigraphic variation of (Pt + Pd + Rh)/(Os + Ir + Ru) for two boreholes, (a) SD45, and (b) GC1, in which all PGE are above detection limits for most samples in the sections. Samples for which any one of the six PGE are below detection limit have not been plotted, resulting in the observed breaks.

(Henderson, 1975; Cawthorn, 1999). These elements were incorporated into the last remnants of the residual melt, finally crystallizing trace minerals rich in these elements (Mathez, 1995; Cawthorn, 1996; Wilson *et al.*, 1999). It is not likely that these late-stage minute crystals would have settled through the semi-rigid cumulus framework, despite their high density.

Absolute concentrations of these trace elements do not represent liquid compositions and instead are largely dependent on how they became incorporated into the final solidified rock. Late-stage processes such as compaction and deformation of the crystal mush, and crystal growth could have caused displacement or migration of the incompatible trace elements.

Highly incompatible elements (Ta, Nb, Th, U; $D < 0{\cdot}001$) would tend to be enriched in the zoned outer rims of the cumulus and oikocrystic phases as their concentrations in the residual melt increase, but slightly less so compared with those incompatible elements that have appreciable partition coefficients (D 0·1–0·01). Elements of this latter type are Zr, Hf and Lu, which, respectively, became preferentially incorporated into pyroxene, and La, which is incorporated into plagioclase. Provided that the highly incompatible elements do not decouple from each other during the crystallization of late-stage minerals, the ratios of these elements could, potentially, provide information on the primary magma composition that formed the cumulates.

Although there are only relatively small changes in the ratios of incompatible elements across the Merensky Reef (Barnes & Maier, 2002; Maier & Barnes, 2005), in detail, and particularly for the thicker reef types, there is discernible small-scale variation. The small-scale systematic variations are interpreted to reflect the involvement of magmas of different compositions that had not completely mixed on the scale of the Merensky pyroxenite. This is consistent with recent Sm–Nd isotopic studies (Prevec *et al.*, 2005; Seabrook *et al.*, 2005) that indicate disequilibrium between coexisting pyroxene and plagioclase, suggesting that they grew from different liquids. Seabrook *et al.* (2005) proposed that the plagioclase and orthopyroxene originated from different magma layers of different compositions, before being juxtaposed after settling. However, they did not consider the effect of continued growth of these phases and further re-equilibration in the final location following settling.

The norite overlying the upper plagioclase pyroxenite has Th/Nb values similar to the Critical Zone magma, whereas the pyroxene-anorthosite underlying the Merensky pyroxenite is closer to the Main Zone magma. This may be seen as supporting the proposal by Seabrook *et al.* (2004, 2005) that the Main Zone magma was emplaced at the base of the Merensky unit and displaced the Critical Zone magma to higher levels in the chamber. However, all of the magmas appear to be hybrids of the two parent magma types to varying degrees and, therefore, the displacement model is probably a simplification of the actual process. This is crucial to understanding the PGE mineralization process.

There is no relationship between the thickness of the Merensky pyroxenite and bulk trace element concentrations. Compaction differences as a means of explaining the variation in reef thickness (Barnes & Maier, 2002) do not, therefore, appear to be an apparent explanation for

these sections. The differences in concentration are entirely due to differences in the amounts of interstitial liquid that were trapped in the cumulates before solidification. Some local redistribution may have taken place by compaction, melt redistribution, and *in situ* fractionation before solidification; this might be indicated by the REE patterns.

REE distributions

The ranges of REE concentrations and pattern-types observed in the Merensky Reef samples appear to be controlled by the combined effect of early formed silicate minerals and late-stage accumulation of interstitial liquid. Continued growth of the primary mineral phases took place from the evolving interstitial liquid, with some possible displacement of that liquid upwards in the crystal pile. Pyroxenes highly enriched in REE have been explained by metasomatic enrichment processes (Mathez, 1995). An alternate model (Cawthorn, 1996) is that the pyroxenes grew from a highly evolved liquid as a result of *in situ* fractionation, a view supported by this study. Recent REE studies on the Bjerkreim–Sokndal intrusion (Charlier *et al.*, 2005) confirmed the reliability of determining liquid compositions from bulk cumulates and indicated that the trapped liquid crystallized as a closed system within the cumulates of that intrusion.

Modelling using a constant magma composition in a single section cannot produce the range of observed REE patterns. The distinctly flatter REE patterns of GC1 and SD22 require a higher proportion of Main Zone type magma, which has a lower $[La/Yb]_N$ than the Critical Zone magma. This is consistent with the higher positive Eu*, particularly for SD22 (Fig. 12) compared with the other sections. The proportion of modelled interstitial liquid (based on the incompatible element distributions shown in Fig. 6) tends to increase upwards in the lower pyroxenite but is generally lower in the upper pyroxenite. The REE patterns characterize distinct layers, indicating the presence of different magmas. Following emplacement of one or more magmas, the evidence suggests that they did not completely mix. It is most likely that cumulus crystals in the different parts of the section nucleated and grew in various discrete combinations of these liquids, resulting from magma mingling. This premise does not contradict the suggestion of Seabrook *et al.* (2005) that cumulus crystals of orthopyroxene settled into a different magma environment from that in which they initially nucleated, and continued to grow from that liquid. This would not have markedly affected the whole-rock incompatible element or REE signatures. The alternation of zones of positive and negative Eu* can be explained by the juxtaposition of liquid layers of different compositions that had also undergone differentiation, probably combined with the interaction of liquid variably depleted by *in situ* crystallization of early formed oikocrystic plagioclase (see Wilson, 1992).

Modelling of the REE patterns of the footwall pyroxene anorthosite and norite is least satisfactory and does not clearly distinguish the relative contributions of the CZ and MZ magmas. The modelled patterns are steeper than observed, and the Eu anomaly is larger.

The concept of mingling and incomplete mixing of magmas is supported by small-scale variations in ratios of incompatible elements, and we propose that the integrity of individual liquid layers is preserved in the Merensky Reef pyroxenite, even though the bulk-rock compositions are not those of the liquids. The relationship between total REE and the highly incompatible trace elements illustrates the roles of different liquids in combination with the cumulus silicate phases. Where the trapped liquid content was very low (1–5%) the REE component was largely controlled by the early formed cumulus silicate phases, which have appreciable partition coefficients for REE. An assemblage of 30% plagioclase and 70% orthopyroxene would have a bulk partition coefficient of ~0·06 for the LREE, rising to 0·27 for Lu. As the amount of trapped liquid increased, the ratio between the total incompatible element and the total REE content became closer to a constant value. With increasing amounts of trapped liquid, Eu* became increasingly negative (as seen in Fig. 12b). This indicates that the trapped liquid dominating the pattern had a negative Eu* signature, which could have been accentuated further by migration of liquid from adjacent layers that had crystallized oikocrystic plagioclase.

The shapes of the REE patterns (expressed as $[La/Yb]_N$) also have a strong relationship to the total incompatible element (Nb + Ta + Th + U) contents (e.g. Fig. 13). In the Merensky pyroxenite, the REE patterns become steeper with increasing amounts of trapped interstitial liquid because of the contrasting influence of the liquid compositions and the partition coefficients for La and Yb in orthopyroxene. REE patterns in pyroxenite with less than 1% trapped liquid have low $[La/Yb]_N$ of 0·1–1. Where the pyroxenes grew in a more evolved liquid (possibly by settling into such a liquid) the REE patterns are flat or U-shaped. The compositions of the cumulates with high proportions of trapped liquid are similar to those of marginal sills considered to represent the Bushveld parental magmas.

The footwall norite has higher $[La/Yb]_N$ as a result of increased cumulus plagioclase content. Contrasting trends in some groups of pyroxenite, in which $[La/Yb]_N$ decreases (yielding flatter REE patterns) with increasing incompatible element content (such as observed in SD46), can be modelled in terms of the relative influence of orthopyroxene, plagioclase and trapped liquid. It is not possible to use a single liquid to model these trends,

and fractionated derivatives of various combinations of the CZ and MZ parental magmas are required. REE patterns in the upper pyroxenite are similar for all sections; in some sections (SD22 and SD45) trace element ratios exhibit less variation, suggesting less heterogeneity in the magma layers. The REE patterns were controlled either by early formed plagioclase competing for space with the trapped liquid, or by more evolved liquid compositions (higher $[La/Yb]_N$) associated with higher levels of incompatible trace elements.

Role of crustal contamination

Recognition of crustal contamination is an important factor in assessing ore-forming processes in large intrusions (Maier & Barnes, 2005). Although magma mixing has been questioned in the formation of Ni–Cu–PGE-rich sulphide bodies (Cawthorn, 2002), the role of crustal contamination remains an important issue in the formation of magmatic sulphide deposits (Maier *et al.*, 2001; Naldrett, 2004).

Trace element ratios complement isotopic data in constraining the petrogenesis and the origin of the magma that formed the Merensky Reef. Inter-element ratios for U, Th, Nb, Ta, Hf and Zr (Table 2) correspond closely to those of the upper crust and are very different to ratios for the lower crust (Rudnick & Gao, 2003) and mantle (Sun & McDonough, 1989). The ratios for the Merensky Reef are intermediate between the values suggested for the CZ (B1) and MZ (B2/B3) parental magmas (Curl, 2001). The trace element data are consistent with a high degree of middle or upper crustal involvement, with contamination most likely to have occurred in a lower holding chamber located at the base of the upper crust. Trace element ratios provide important evidence on the genesis of the magmas, and reflect the fine-scale structure within the cumulus pile. However, we consider it unlikely that crustal contamination *per se* gave rise to sulphide formation in the Merensky Reef.

Distribution of sulphide

As is typical for pyroxenite of this type (such as in the Great Dyke of Zimbabwe), plagioclase occurs as large oikocrysts or as a heteradcumulate phase (Wager & Brown, 1968) formed by liquidus-stage growth, slightly later than that of orthopyroxene (Wilson, 1992); it, therefore, commonly encloses orthopyroxene crystals. The role of interstitial plagioclase is important in that it may influence the crystal matrix and control the distribution of both sulphide and silicate liquid.

Sulphide appears to have concentrated in those regions where plagioclase did not crystallize as early formed oikocrysts. The concentration of immiscible sulphide liquid was dependent on the relative distribution and amount of trapped interstitial silicate liquid, but in itself was not responsible for the formation of the sulphide. Similar relationships have been demonstrated in the Main Sulphide Zone of the Great Dyke (Wilson & Brown, 2005). Early formed plagioclase, either as cumulate crystals or as early formed oikocrysts, strongly influenced the accumulation and distribution of interstitial trapped liquid, and, therefore, also the distribution of sulphide liquid.

Magmas that are initially S-undersaturated can become S-saturated through either differentiation of magma or cooling, or both, and the sulphide formed can scavange PGE from the magma to form PGE deposits (Keays, 1995). The Merensky Reef is considered by some workers to be close to the boundary at which the Bushveld magma became S-saturated, with the great thickness of the overlying Main Zone magma having been stripped of its PGE content (Maier & Barnes, 2005). However, there is no evidence from the PGE contents and tenors that the Main Zone (MZ) magma had an appreciable PGE content before it was emplaced. The role of sulphide in stripping the large volume of residual magma in the chamber of its PGE content should, therefore, be questioned.

Mechanisms for the origin of the Merensky Reef and its PGE mineralization

Hypotheses for the origin of the Merensky Reef are wide-ranging and draw on many critical observations of textures, rock and mineral compositions, possible interactions between solid and liquid, and between possible liquids. There is currently little consensus as to which model best explains the formation of the Merensky pyroxenite and its PGE mineralization. Models have ranged from complete magma mixing (Campbell *et al.*, 1983) to the role of fluids and volatiles (Boudreau *et al.*, 1986), or the progressive passage of a hydration or melting front (Nicholson & Mathez, 1991). On the basis of contradictory evidence from isotopic analyses of cumulus and intercumulus phases (Seabrook *et al.*, 2004, 2005) mixing of magmas does not provide a satisfactory explanation for the mineralization process and alternative (unspecified) mechanisms should be sought. Rb is generally considered to be a highly mobile element and, therefore, the influence of fluid in the formation of the rock-types or the mineralization would be expected to have caused dispersion of this element. The strong correlation of mobile elements [Rb (Fig. 8) and Cs; A. Wilson, unpublished data] with the incompatible (and generally immobile) elements indicates that extensive fluid migration did not occur, but limited-scale redistribution by late-stage hydrous fluids cannot be ruled out.

Many other studies have proposed or reviewed possible mechanisms of PGE enrichment (Naldrett *et al.*, 1986; Lee, 1996; Cawthorn, 1999). There is persuasive evidence from Sr isotopic studies that magma mixing (or interaction) took place in the vicinity of the Merensky pyroxenite (Kruger & Marsh, 1982; Kruger, 1994), close to the transition of the Critical and Main Zones, but it has yet to be proved that this mixing was responsible for the sulphide and PGE mineralization. Mixing of different magmas has been proposed to explain the precipitation of sulphide (Campbell *et al.*, 1983; Naldrett *et al.*, 1987; Li *et al.*, 2001*a*, 2001*b*) and subsequent entrapment of PGE as a result of their highly efficient partitioning into sulphide (Peach *et al.*, 1990). The question of sulphide precipitation by these mechanisms has been questioned on the basis of the nature of the sulphide saturation curve for silicate magmas (Cawthorn, 2002). A further difficulty (Ballhaus & Ryan, 1995) for such a mixing model is that the relative PGE abundances observed in the Merensky Reef are similar to those in the proposed parent melts (Davies & Tredoux, 1985). Given the exceptionally high enrichment factors of PGE required to produce the Merensky Reef sulphides, distribution patterns for these elements should more closely reflect their partition coefficients between sulphide and silicate liquid (Ballhaus & Ryan, 1995), but this is not observed. Ballhaus & Ryan (1995) demonstrated that PGE clusters formed in the magma are likely to have played a significant role in the formation of the Merensky Reef.

Sm–Nd isotopic evidence indicates that crystals of pyroxene and plagioclase were derived from liquids of different compositions (Prevec *et al.*, 2005; Seabrook *et al.*, 2005). These different magma layers are postulated to have arisen from the emplacement of the Main Zone magma into an existing evolved Critical Zone magma. As noted earlier, the trace element distributions demonstrated from this study support the concept that mingling, but incomplete mixing, of magmas occurred at the level of the Merensky pyroxenite. The observed differences in the cumulate sequence are here attributed to mainly preserved liquid signatures, with a possible influence of cumulate crystals that settled into liquids that were different from those in which they initially nucleated. Trapped liquid has a greater control on the incompatible trace element composition than the cumulus crystals and, therefore, closely reflects the composition of the liquid.

Attention has also focused on the unusual compositions of the Merensky Reef in terms of its trace mineralogy (Ohnenstetter *et al.*, 1998; Arndt *et al.*, 2005). The abnormally high sulphide content has prompted the suggestion that the Merensky Reef was a one-off event resulting from the emplacement of an unusual metal-rich magma (Lee & Butcher, 1990; Lee, 1996; Maier *et al.*, 2000; Arndt *et al.*, 2005). Our results do not support such a view, as the distributions of trace elements can, for the most part, be explained by modelling of currently accepted parental magma compositions. The trace mineral assemblages are largely due to the final component of crystallized trapped liquid, which has been shown to vary greatly between sections.

Distribution of PGE in relation to rock type

There is no relationship between PGE distributions and changes in whole-rock composition, except that the concentration of metals occurs towards the top of the lower pyroxenite close to, but seldom exactly coinciding with the top chromitite. PGE are also concentrated in a narrow interval at the base of the pyroxenite, usually in association with a thin chromitite layer. The major portion of the mineralized zone is, therefore, not related to any specific rock layer. The observed close association of PGE mineralization with sulphide, similarity of patterns of variation between total and individual PGE with S, and the overall linearity in cumulative plots indicate that sulphide was responsible for the collection and concentration of PGE in all sections. Sulphide probably formed as an immiscible liquid that became redistributed within the pyroxene cumulate. Mobile elements (K and Rb) provide no evidence in these sections of extensive fluid migration that might have redistributed the PGE.

There is no evidence through the entire sequence of the Merensky pyroxenite that progressive fractional segregation of the PGE, as a result of sulphide separation, took place from a single liquation event, as observed in other PGE deposits (most notably the Great Dyke; Prendergast & Keays, 1989; Wilson *et al.*, 1998; Naldrett, 2004). However, the marked decrease of total PGE and PGE tenor, and increase of Pt/Pd upwards in the upper pyroxenite do indicate fractional segregation of sulphide similar to that observed in the Great Dyke. The contrasting characteristics observed in the lower and upper pyroxenites indicate that different processes controlled the mineralization in these sections. The PGE distributions may, therefore, be characterized into two distinct types: dynamically controlled emplacement in the lower pyroxenite, and fractionation control in the upper pyroxenite. Fractionation is attributed to the high partition coefficients for PGE between sulphide liquid and silicate magma, and to D_{Pd} being greater than D_{Pt} (Naldrett *et al.*, 1990; Peach & Mathez, 1996). In the upper part of the lower pyroxenite the total PGE content and PGE tenor increase upwards and Pt/Pd decreases. This may indicate a dynamic system in which S and PGE-undepleted magma was entering the zone at the same time that sulphide was precipitating. That the total amounts of sulphide and PGE appear to be related to the

thickness of the pyroxenite unit (for a specific area) indicates a direct genetic link between the mineralization and the rock-forming process.

It has been shown in previous studies (Kruger & Marsh, 1982; Prevec *et al.*, 2005) that the Main Zone magma was probably involved in the emplacement of the Merensky pyroxenite, but that cumulus minerals with Critical Zone magma signatures also occur higher in the succession (Seabrook *et al.*, 2004). The whole-rock trace element signatures from this study indicate that the final bulk compositions of the entire sequence are intermediate between the two parental magma compositions, with overall stronger affinities to the Critical Zone magma. Cumulus crystals could have been derived from several different magma layers and settled into other layers dominated by one or the other of the two magmas, or incompletely mixed magma layers. These crystals would have continued to equilibrate with the enclosing magma. Therefore, it also likely that the cumulus crystals reflect the complex history of the juxtaposed liquid layers.

Trends of PGE tenor and Pt/Pd through the sequence indicate that controls other than crystal–liquid fractionation were involved in the formation of the mineralization. The small-scale variation of these parameters, and their correspondence to changes in the ratios of incompatible trace elements, suggests control by a common mechanism. The apparent dependence between total metal contents (PGE and base metals), amount of sulphide, thickness of the Merensky pyroxenite and trace element signatures suggests a common genetic link.

A model for the Merensky unit

Early studies (Kruger & Marsh, 1982) proposed that the Merensky pyroxenite possessed Sr-isotope signatures intermediate between those of the Critical Zone and Main Zone magmas. The term 'Transitional Zone' (Kruger, 1990) was suggested as being more appropriate for the interval encompassing the Merensky Reef and overlying Bastard Reef units. Seabrook *et al.* (2004, 2005) proposed that this transition arose because of the emplacement of the Main Zone magma into the chamber at the base of the existing Critical Zone magma; however, this model in itself does not explain the reversal to abundant orthopyroxene crystallization that formed the Merensky pyroxenite with a strong Critical Zone signature. A further influx of Critical Zone magma is also required at this level.

In this respect it is instructive to consider the crystallization temperatures and liquid compositions that can be modelled using the MELTS program (Ghiorso & Sack, 1995). Crystallization of the CZ magma [with 12·4% MgO—selected on the basis of the most likely liquid compositions from Curl (2002), and the suggested putative Lower Zone magma of Davies *et al.* (1980)] is predicted to commence at 1366°C yielding orthopyroxene on the liquidus of En_{89}. The observed Mg-number of the Merensky pyroxenite largely reflects the composition of the orthopyroxene and is indicated to be about 0·80, with some compositions as high as 0·82. These compositions do not take into account the re-equilibration of the orthopyroxene with the trapped liquid (Barnes, 1986). The change as a result of re-equilibration has been shown to modify the original liquidus orthopyroxene compositions by 0·01–0·02 En units (Wilson, 2001). Therefore, the liquidus orthopyroxene compositions are likely to have been about En_{83}. Such a composition is modelled by MELTS to appear at 1250°C as a result of mixing of evolved resident CZ magma, with the influx of new CZ magma. The B2 magma is predicted to have started crystallizing at about 1220°C, with both plagioclase and clinopyroxene on the liquidus. The interaction of these magmas would have had the effect of rapidly cooling the resident CZ magma.

Consistent with recent isotopic studies (Prevec *et al.*, 2005; Seabrook *et al.*, 2005), it is proposed that the Merensky pyroxenite is the result of crystallization of magmas that had mingled but not mixed, and that the cumulus crystals and interstitial minerals were derived from complex associations of these different liquids. Discrete layers of the contrasting magmas may have existed. Emplacement of the Critical Zone magma in association with, or followed shortly later by, a batch of Main Zone magma, would have given rise to marked compositional heterogeneity and strong local thermal gradients. The cooling effect of the Main Zone magma on the resident Critical Zone magma, which was close to sulphide saturation and rich in PGE [as indicated by the compositions of the marginal sills (Davies & Tredoux, 1985)], could, therefore, have caused the precipitation of sulphide as immiscible droplets from that magma giving rise to the Merensky Reef. Embryonic clusters of PGE in close association with sulphide and semi-metals (As, Te) were probably already formed in the residual Critical Zone magma at that stage (Tredoux *et al.*, 1995; Ballhaus & Sylvester, 2000), which were then scavenged by the sulphide droplets. Continued emplacement of the Main Zone magma caused the sustained undercooling of the Critical Zone magma required to crystallize orthopyroxene in the Merensky pyroxenite. Cumulus crystals may also have re-equilibrated with different magmas from those in which they initially nucleated.

In various local environments the physical interaction of the Critical Zone and Main Zone magmas would have been highly variable, resulting in the different observed characteristics of the Merensky Reef in different areas. The pegmatoidal facies of the Merensky Reef has previously been interpreted as resulting from

undercooling of the new magma (Ballhaus & Ryan, 1995). The chilling of the CZ magma could explain such features as harrisitic olivine growth and the presence of fine-grained pyroxenite layers, as described for these sections.

Variable rates of cooling and crystallization could have given rise to markedly different amounts of trapped liquid in the various Merensky Reef sections. Relatively rapid crystallization of higher-temperature magma associations (higher Mg-number) were most effective in trapping interstitial liquid, as indicated by the relationship of incompatible elements and Mg-number of the rock. It is unlikely that these controls would have been the same in all areas of the Bushveld magma chamber. Additional factors would include the location of feeder zones, as well as progressive lateral and down-dip facies variations, and the proximity to the wall- or floor-rocks of the intrusion. These differences may have given rise to economically distinct areas (geozones) with different PGE contents, metal distributions and sulphide tenors.

Much detailed work in many areas of the Bushveld Complex remains to be done before the Merensky Reef is fully understood.

ACKNOWLEDGEMENTS

This work was supported by the National Research Foundation (South Africa) through the THRIP (Technology and Human Resources for Industry Programme) and Anglo Platinum. Anglo Platinum is thanked for permission to publish this paper. We thank Tony Naldrett, Richard Arculus and an anonymous referee for constructive criticisms of the manuscript. Dr Chris Lee is acknowledged for mentoring this project and for much stimulating discussion. The authors take full responsibility for the deductions and conclusions in this paper.

SUPPLEMENTARY DATA

Supplementary data for this paper are available at *Journal of Petrology* online.

REFERENCES

Arndt, N., Jenner, G., Ohnenstetter, M., Deloule, E. & Wilson, A. H. (2005). Trace elements in the Merensky Reef and adjacent norites, Bushveld Complex, South Africa. *Mineralium Deposita* **40**, 550–575.

Asimow, P. D. & Langmuir, C. H. (2003). The importance of water to oceanic mantle melting regimes. *Nature* **421**, 815–820.

Ballhaus, C. & Ryan, C. G. (1995). Platinum-group elements in the Merensky reef. I. PGE in solid solution in base metal sulphides and the down-temperature equilibration of Merensky ores. *Contributions to Mineralogy and Petrology* **122**, 241–251.

Ballhaus, C. & Sylvester, P. (2000). Noble metal enrichment processes in the Merensky Reef, Bushveld Complex. *Journal of Petrology* **41**, 545–561.

Barnes, S. J. (1986). The effect of trapped liquid crystallization on cumulus mineral compositions in layered intrusions. *Contributions to Mineralogy and Petrology* **93**, 524–531.

Barnes, S.-J. & Maier, W. D. (1999). The fractionation of Ni, Cu and the noble metals in silicate and sulfide liquids. In: Keays, R. R. (ed.) *Dynamic Processes in Magmatic Ore Deposits and their Application in Mineral Exploration. Geological Association of Canada, Short Course Notes* **13**, 69–106.

Barnes, S.-J. & Maier, W. D. (2002). Platinum-group elements and micro-structures of normal Merensky reef from Impala Platinum Mines, Bushveld Complex. *Journal of Petrology* **43**, 103–128.

Blundy, J. & Wood, B. J. (2003). Partitioning of trace elements between crystals and melt. *Earth and Planetary Science Letters* **210**, 383–397.

Boudreau, A. E. & McCullum, I. S. (1992). Concentration of platinum-group elements by magmatic fluids in layered intrusions. *Economic Geology* **87**, 1830–1848.

Boudreau, A. E. & Meurer, W. P. (1999). Chromatographic separation of the platinum-group elements, gold, base metals and sulfur during degassing of a compacting and solidifying igneous crystal pile. *Contributions to Mineralogy and Petrology*, **134**, 174–185.

Boudreau, A. E., Mathez, E. A. & McCullum, S. (1986). Halogen geochemistry of the Stillwater and Bushveld Complexes: evidence for transport of the platinum-group elements by Cl-rich fluids. *Journal of Petrology* **27**, 967–986.

Brown, R. T. (2004). Mafic and ultramafic rocks of the Bushveld Complex: a note on their classification and nomenclature. Anglo Platinum Internal Report, 77 pp.

Buick, I. S., Maas, R. & Gibson, R. (2001). Precise U–Pb titanite age constraints on the emplacement age of the Bushveld Complex, South Africa. *Journal of the Geological Society, London* **158**, 3–6.

Campbell, I. H., Naldrett, A. J. & Barnes, S. J. (1983). A model for the origin of the platinum-rich sulphide horizons in the Bushveld and Stillwater Complexes. *Journal of Petrology* **24**, 133–185.

Cawthorn, R. G. (1996). Models for incompatible trace element abundances in cumulus minerals and their application to plagioclase and pyroxenes in the Bushveld Complex. *Contributions to Mineralogy and Petrology* **123**, 109–115.

Cawthorn, R. G. (1999). Platinum-group element mineralization of the Bushveld Complex—a critical reassessment of geochemical models. *South African Journal of Geology* **102**, 268–281.

Cawthorn, R. G. (2002). The role of magma mixing to the genesis of PGE mineralization in the Bushveld Complex: thermodynamic calculations and new interpretations—a discussion. *Economic Geology* **97**, 663–667.

Cawthorn, R. G. & Davies, G. (1983). Experimental data at 3 kbars pressure on parental magma to the Bushveld Complex. *Contributions to Mineralogy and Petrology* **83**, 128–135.

Cawthorn, R. G., Davies, G., Clubley-Armstrong, A. & McCarthy, T. S. (1981). Sills associated with the Bushveld Complex, South Africa: an estimate of parental magma composition. *Lithos* **14**, 1–16.

Charlier, B. J. & Duchesne, J.-C. (2005). Geochemistry of cumulates from the Bjerkreim–Sokndal Intrusion (S. Norway) Part II. REE and the trapped liquid fraction. *Lithos* **83**, 255–276.

Curl, E. A. (2001). Parental magmas to the Bushveld Complex, South Africa. Ph.D. thesis. Monash University, 140 pp.

Davies, G. & Tredoux, M. (1985). The platinum-group element and gold contents of marginal rocks and sills of the Bushveld Complex. *Economic Geology* **80**, 838–848.

Davies, G., Cawthorn, R. G., Barton, J. M. J. & Morton, M. (1980). Parental magma to the Bushveld Complex. *Nature* **287**, 33–35.

Donaldson, C. H. (1974). Olivine crystal types in harrisitic rocks of the Rhum pluton and Archean spinifex. *Geological Society of America Bulletin* **85**, 1721–1726.

Eales, H. V. (2002). Caveats in defining the magmas parental to the mafic rocks of the Bushveld Complex, and the manner of their emplacement: review and commentary. *Mineralogical Magazine* **66**, 815–832.

Eales, H. V. & Cawthorn, R. G. (1996). The Bushveld complex. In: Cawthorn, R. G. (ed.) *Layered Intrusions*. Amsterdam: Elsevier, pp. 181–230.

Ghiorso, M. S. & Sack, R. O. (1995). Chemical mass transfer in magmatic processes. IV. A revised and internally consistent thermodynamic model for the interpolation and extrapolation of liquid–solid equilibria in magmatic systems at elevated temperatures and pressures. *Contributions to Mineralogy and Petrology* **119**, 197–212.

Gillespie, M. R. & Styles, M. T. (1999). *BGS Rock Classification Scheme Volume 1: Classification of Igneous Rocks. British Geological Survey Research Report RR99-06*. Keyworth: British Geological Survey, 52 pp.

Green, T. H. (1994). Experimental studies of trace-element partitioning applicable to igneous petrogenesis—Sedona 16 years later. *Chemical Geology* **117**, 1–36.

Green, T. H. & Pearson, N. J. (1985). Rare earth element partitioning between clinopyroxene and silicate liquid at moderate to high pressure. *Contributions to Mineralogy and Petrology* **91**, 24–36.

Harmer, R. E. & Sharpe, M. R. (1985). Field relations and strontium isotope systematics of the marginal rocks of the eastern Bushveld Complex. *Economic Geology* **80**, 813–837.

Henderson, P. (1975). Geochemical indicator of the efficiency of fractionation of the Skaergaard intrusion, east Greenland. *Mineralogical Magazine* **40**, 285–291.

Irvine, T. N. & Sharpe, M. R. (1983). Source-rock compositions and depths of origin of Bushveld and Stillwater magmas. *Carnegie Institution of Washington Yearbook—Papers from the Geophysical Laboratory* **80**, 294–303.

Johannsen, A. (1931). *A Descriptive Petrography of the Igneous Rocks, Volume 1*. Chicago, IL: University of Chicago Press, 267 pp.

Keays, R. R. (1995). The role of komatiitic and picritic magmatism S-saturation in the formation of ore deposits. *Lithos* **34**, 1–18.

Kruger, F. J. (1990). The stratigraphy of the Bushveld Complex: a reappraisal and the relocation of the Main Zone boundaries. *South African Journal of Geology* **93**, 376–381.

Kruger, F. J. (1994). The Sr-isotope stratigraphy of the western Bushveld Complex. *South African Journal of Geology* **97**, 393–398.

Kruger, F. J. (2005). Filling the Bushveld Complex magma chamber: lateral expansion, roof and floor interaction, magmatic unconformities, and the formation of giant chromitite, PGE and T-V-magnetitite deposits. *Mineralium Deposita* **40**, 451–472.

Kruger, F. J. & Marsh, J. S. (1982). Significance of $^{87}Sr/^{86}Sr$ ratios in the Merensky cyclic unit of the Bushveld Complex. *Nature* **298**, 53–55.

Lee, C. A. (1996). A review of mineralization in the Bushveld Complex, and some other layered mafic intrusions. In: Cawthorn, R. G. (ed.) *Layered Intrusions*. Amsterdam: Elsevier, pp. 103–146.

Lee, C. A. & Butcher, A. R. (1990). Cyclicity in Sr-isotopic stratigraphy through the Merensky and Bastard reef units, Atok section, eastern Bushveld Complex. *Economic Geology* **85**, 173–190.

Leeb-du Toit, T. A. (1986). The Impala Platinum Mines. In: Anhaeusser, C. R. & Maske, S. (eds) *Mineral Deposits of Southern Africa*. Johannesburg: Geological Society of South Africa, pp. 1091–1106.

Le Maitre, R. W. (1989). *A Classification of Igneous Rocks and Glossary of Terms*. Oxford: Blackwell Scientific, 193 pp.

Li, C., Maier, W. D. & de Waal, S. A. (2001a). The role of magma mixing to the genesis of PGE mineralization in the Bushveld Complex: thermodynamic calculations and new interpretations. *Economic Geology* **96**, 653–662.

Li, C., Maier, W. D. & de Waal, S. A. (2001b). The role of magma mixing to the genesis of PGE mineralization in the Bushveld Complex: thermodynamic calculations and new interpretations—erratum. *Economic Geology* **96**, 1487.

Maier, W. D. & Barnes, S.-J. (1999). Platinum-group elements in silicate rocks of the lower, critical and main zones at Union Section, western Bushveld Complex. *Journal of Petrology*, **10**, 1647–1671.

Maier, W. D. & Barnes, S.-J. (2005). Application of lithogeochemistry to exploration for PGE deposits. In: Mungall, J. E. (ed.) *Exploration for Platinum Group Element Deposits*. Ottawa, Ont.: Mineralogical Association of Canada, pp. 309–333.

Maier, W. D., Arndt, N. T. & Curl, E. (2000). Progressive crustal contamination of the Bushveld Complex: evidence from Nd analyses of the cumulus rocks. *Contributions to Mineralogy and Petrology* **140**, 316–327.

Maier, W. D., Barnes, S.-J. & Li, C. (2001). A re-evaluation of the role of crustal contamination in the formation of magmatic sulfides in the Bushveld Complex. In: Boudreau, A. (ed.) *9th International Platinum Symposium*. Billings, Montana: Durham, Duke University, pp. 283–285.

Mathez, E. A. (1995). Magmatic metasomatism and formation of the Merensky reef, Bushveld Complex. *Contributions to Mineralogy and Petrology* **119**, 277–286.

McDade, P., Blundy, J. D. & Wood, B. J. (2003). Trace element partitioning between mantle wedge peridotite and hydrous MgO-rich melt. *American Mineralogist* **88**, 1825–1831.

McKenzie, D. & O'Nions, R. K. (1991). Partial melt distributions from inversion of rare earth element concentrations. *Journal of Petrology* **32**, 1021–1091.

Naldrett, A. J. (2004). *Magmatic Sulfide Deposits*. Berlin: Springer, 727 pp.

Naldrett, A. J. & Wilson, A. H. (1990). Horizontal and vertical variations in noble metals in the Great Dyke of Zimbabwe: a model for the origin of PGE mineralization by fractional segregation. *Chemical Geology* **88**, 279–300.

Naldrett, A. J., Gasparrini, E. C., Barnes, S. J., von Gruenewaldt, G. & Sharpe, M. R. (1986). The upper critical zone of the Bushveld Complex and the origin of Merensky-type ores. *Economic Geology* **81**, 1105–1117.

Naldrett, A. J., Cameron, G., von Gruenewaldt, G. & Sharpe, M. R. (1987). The formation of stratiform PGE deposits in layered intrusions. In: Parsons, I. (ed.) *Origins of Igneous Layering*. Dordrecht: D. Reidel, pp. 313–398.

Naldrett, A. J., Brugmann, G. E. & Wilson, A. H. (1990). Models for the concentration of PGE in layered intrusions. *Canadian Mineralogist*, **28**, 389–408.

Nicholson, D. M. & Mathez, E. D. (1991). Petrogenesis of the Merensky Reef in the Rustenburg section of the Bushveld Complex. *Contributions to Mineralogy and Petrology*, **107**, 293–309.

Nielsen, R. (2004). http://earthref.org/GERM/tools/tep.htm.

Ohnenstetter, M., Arndt, N., Lee, C. A. & Wilson, A. H. (1998). Occurrence and compositional variation of HFSE and LILE-bearing oxides in the Merensky Reef, Rustenburg area. In: *8th International Platinum Symposium*. Johannesburg: South African Institute of Mining and Metallurgy, pp. 301–304.

Peach, C. L. & Mathez, E. A. (1996). Constraints on the formation of platinum-group element deposits in igneous rocks. *Economic Geology* **91**, 439–450.

Peach, C. L., Mathez, E. A. & Keays, R. R. (1990). Sulfide melt–silicate melt distribution coefficients for noble metals and other chalcophile elements as deduced from MORB: implications for partial melting. *Geochimica et Cosmochimica Acta* **54**, 3379–3389.

Prendergast, M. D. & Keays, R. R. (1989). Controls of platinum-group element mineralization and the origin of the PGE-rich Main Sulphide Zone in the Wedza Subchamber of the Great Dyke, Zimbabwe: implications for the genesis of, and exploration for, stratiform PGE mineralization in layered intrusions. In: Prendergast, M. D. & Jones, M. J. (eds) *Magmatic Sulphides—the Zimbabwe Volume*. London: Institution of Mining and Metallurgy, pp. 43–69.

Prevec, S. A., Ashwall, L. D. & Mkaza, M. Z. (2005). Mineral disequilibrium in the Merensky Reef, western Bushveld Complex, South Africa: new Sm–Nd isotopic evidence. *Contributions to Mineralogy and Petrology* **149**, 306–325.

Rollinson, H. (1993). *Using Geochemical Data*. New York: John Wiley, 352 pp.

Rudnick, R. L. & Gao, S. (2003). Rudnick, R. L. (2003). Composition of the continental crust. *The Crust. Treatise on Geochemistry*. Oxford: Elsevier–Pergamon, pp. 1–64.

SACS (1980). Lithostratigraphy of the Republic of South Africa, South West Africa/Namibia, and the Republics of Bophuthatswana, Transkei and Venda. In: Kent, L. E. (ed.) *Stratigraphy of South Africa, Part 1*. Pretoria: Geological Survey of South Africa, p. 690.

Schoenberg, R., Kruger, F. J., Nagler, T. F., Meisel, T. & Kramers, J. D. (1999). PGE enrichment in chromitite layers and the Merensky Reef of the western Bushveld Complex: a Re–Os and Rb–Sr isotope study. *Earth and Planetary Science Letters* **172**, 49–64.

Seabrook, C. L., Cawthorn, R. G. & Kruger, F. J. (2004). Geochemical disequilibrium in the Merensky and Bastard reefs, eastern Bushveld Complex: co-accumulation of minerals from stratified magmas. In: Ashwall, L. D. (ed.) *Geoscience Africa 2004*. School of Geosciences, University of the Witwatersrand, Johannesburg, pp. 584–585.

Seabrook, C. L., Cawthorn, R. G. & Kruger, F. J. (2005). The Merensky Reef, Bushveld Complex: mixing of minerals not mixing of magmas. *Economic Geology* **100**, 1191–1206.

Sharpe, M. R. (1981). The chronology of magma influxes to the eastern compartment of the Bushveld Complex as exemplified by its marginal border groups. *Journal of the Geological Society, London* **138**, 307–326.

Sharpe, M. R. & Hulbert, L. J. (1985). Ultramafic sills beneath the eastern Bushveld Complex. *Economic Geology* **80**, 849–871.

Sun, S.-s. & McDonough, W. F. (1989). Chemical and isotopic systematics of oceanic basalts: implications for mantle composition and processes. In: Saunders, A. D. & Norry, M. J. (eds) *Magmatism in the Ocean Basins. Geological Society, London, Special Publications* **42**, 313–345.

Tredoux, M., Lindsay, N. M., Davies, G. & McDonald, I. (1995). The fractionation of platinum-group elements in magmatic systems, with the suggestion of a novel causal mechanism. *South African Journal of Geology* **98**, 157–167.

Viljoen, M. J. (1999). The nature and origin of the Merensky Reef of the western Bushveld Complex based on geological and geophysical data. *South African Journal of Geology* **102**, 221–239.

Viljoen, M. J. & Hieber, R. W. (1986). The Rustenburg section of Rustenburg Platinum Mines Limited, with reference to the Merensky Reef. In: Anhaeusser, C. R. & Maske, S. (eds) *Mineral Deposits of Southern Africa 2*. Johannesburg: Geological Society of South Africa, pp. 1061–1090.

Viljoen, M. J. & Schurmann, L. W. (1998). Platinum group metals. In: Wilson, M. G.C. & Anhaeusser, C. R. (eds) *The Mineral Resources of South Africa*. Pretoria: Council for Geoscience, pp. 532–568.

Wager, L. R. & Brown, G. M. (1968). *Layered Igneous Rocks*. Edinburgh: Oliver and Boyd, 588 pp.

Walraven, F., Armstrong, R. A. & Kruger, F. J. (1990). A chronostratigraphic framework for the north–central Kaapvaal Craton, Bushveld Complex and Vredefort Structure. *Tectonophysics,* **171**, 23–48.

Wilson, A. H. (1992). The geology of the Great Dyke, Zimbabwe: crystallization, layering, and cumulate formation in the P1 Pyroxenite of cyclic unit 1 of the Darwendale Subchamber. *Journal of Petrology* **33**, 611–663.

Wilson, A. H. (2001). Compositional and lithological controls on the PGE-bearing sulphide zones in the Selukwe Subchamber, Great Dyke: a combined equilibrium–Rayleigh fractionation model. *Journal of Petrology* **42**, 1845–1867.

Wilson, A. H. & Brown, R. T. (2005). Exploration and mining perspective of the Main Sulfide Zone of the Great Dyke, Zimbabwe—case study of the Hartley Platinum Mine. In: Mungall, J. (ed.) *Exploration for Platinum Group Element Deposits. Mineralogical Association of Canada, Short Course Notes* **35**, 409–429.

Wilson, A. H. & Tredoux, M. (1990). Lateral and vertical variation of the platinum-group elements, and petrogenetic controls on the sulphide mineralization in the P1 Pyroxenite Layer of the Darwendale Subchamber of the Great Dyke, Zimbabwe. *Economic Geology* **85**, 556–584.

Wilson, A. H., Dawson, S. & Murahwi, C. Z. (1998). Decoupling of nickel and major elements in olivine from the Bushveld Complex and Great Dyke: study of sulfide control. In: *Abstracts: International Mineralogical Association, 17th Annual General Meeting*. Mineralogical Association of Canada, Toronto, p. A6.

Wilson, A. H., Lee, C. A. & Brown, R. T. (1999). Geochemistry of the Merensky Reef, Rustenburg Section, Bushveld Complex: controls on the silicate framework and distribution of sulphide and trace elements. *Mineralium Deposita* **34**, 657–672.

Wilson, A. H., Jermy, C. A., Ridgeway, M. & Chunnett, G. (2005). Rock-strength and physical properties of norites of the Merensky and Bastard units, Western Bushveld Complex. *South African Journal of Geology* **108**, 525–540.